

1
2
3
4
5
6
7
8
9
10
11
12
13
14
15
16
17

**Genesis of chromium-rich kyanite in eclogite-facies Cr-spinel-bearing gabbroic
cumulates, Pohorje Massif, Eastern Alps**

Christoph A. Hauzenberger¹, Harald Taferner¹, and Jürgen Konzett²

¹ Institute of Earth Sciences, Karl-Franzens-University of Graz, Universitaetsplatz 2, Graz, 8010,
Austria

² Institute of Mineralogy und Petrography, University of Innsbruck, Innrain 52, Innsbruck, 6020,
Austria

Revision 1

18 **ABSTRACT**

19 Natural kyanites with Cr₂O₃ contents >1 wt% are very rare and known only from high-P environments.
20 One example are eclogite-facies gabbroic cumulates containing Cr-spinel from the Pohorje Massif,
21 Eastern Alps, Slovenia. In these rocks turquoise coloured Cr-rich kyanites are present in two different
22 textural types: A first type has formed as blocky crystals of several hundred μm in size around clusters
23 of small drop-like Cr-spinels. This kyanite shows a highly irregular Cr distribution and may contain up
24 to 15.6 wt% Cr₂O₃ which is one of the highest Cr₂O₃ contents reported so far. A second type is present
25 as part of reaction coronas around large red-brownish Cr-spinel and forms deep-blue needle-like
26 crystals which rarely exceed 100 μm in size. This kyanite contains up to 8.2 wt% Cr₂O₃ and is
27 associated with Cr-rich corundum (≤ 9.1 wt% Cr₂O₃) and Cr-Al-rich pargasite (≤3.9 wt% Cr₂O₃). The
28 formation of kyanite around Cr-spinel droplets is interpreted to be the result of increasing *PT*
29 conditions during prograde metamorphism where Cr-spinel and plagioclase or quartz react to Cr-
30 kyanite, ±garnet, ±omphacite. In contrast, the formation of kyanite associated with Cr-rich corundum
31 and Cr-rich pargasite within coronas around Cr-spinel occurred in an early stage of the retrogressive
32 evolution of the gabbroic cumulates at eclogite-facies conditions of ~2.5 GPa and 750 – 800°C
33 triggered by the influx of H₂O-rich fluids. The driving force for developing these coronas was an
34 increase in the chemical potential of silica caused by the infiltrating hydrous fluid phase. *PT* estimates
35 using matrix mineral assemblage place the peak metamorphic conditions close to the quartz/coesite
36 transition with temperatures in the range of 750–810°C and pressures of ~2.9 GPa.

37

38 **Keywords:** Cr-rich kyanite, Cr-rich corundum, eclogite facies cumulates, Pohorje Massif,

39

40

INTRODUCTION

41
42 Kyanite is a common metamorphic mineral in metapelites and Al-rich metabasites at medium to
43 high pressures and can accommodate substantial amounts of manganese, iron (e.g. Chinner et al. 1969;
44 Grambling and Williams 1984) and especially chromium in its crystal structure. Cr–Al substitution
45 results in a spectacular turquoise-blue color and strong pleochroism as reported by Sobolev (1968),
46 Cooper (1980), and Gil-Ibarguchi (1991). Cr–Al substitution in synthetic kyanite, on the other hand,
47 produces a deep emerald green color (Langer and Seifert 1974). This suggests that the blue color of
48 natural Cr-bearing kyanite results from a combination of Cr and additional minor substituents such as
49 Fe and/or Ti (White and White 1967; Rost and Simon 1972). Natural kyanite with Cr₂O₃ contents >1
50 wt% have been known so far only from high-P environments. The highest Cr₂O₃ content documented
51 in the literature so far is 15.7 wt% which corresponds to ~18 mol% Cr₂SiO₅ component and was
52 reported by Negulescu and Sabau (2012) from chromite-bearing meta-gabbroic eclogites. Kyanite with
53 up to 12.7 and 11.8 wt% Cr₂O₃ were reported by Sobolev et al. (1968) and Pivin et al. (2011) from
54 kimberlite-derived grosspydrite and clinopyroxenite nodules. Kyanite with up to 25 mol% Cr₂SiO₅ was
55 synthesized by Langer and Seifert (1974) at 3 GPa and 1300-1500°C. These authors suggested that
56 significant amounts of Cr can enter the kyanite structure only at $P \geq 1.8$ GPa and $T \geq 900^\circ\text{C}$ and that the
57 amount of Cr incorporated is positively correlated with both P and T . A comparison with PT conditions
58 of equilibration estimated for Cr-kyanite-bearing eclogite from the South Carpathians by Negulescu
59 and Sabau 2012 shows that whereas high pressures are indeed essential, temperatures as low as 600°C
60 are sufficient to allow substantial Al–Cr substitution. Hence, high pressures in excess of ~2GPa and a
61 suitable source of Cr which is usually Cr-spinel are essential pre-requisites for the formation of Cr-rich
62 kyanite.
63

64 Eclogites within the Eastern alpine crystalline basement typically appear as lenses and small
65 bodies of up to several hundred meters in size within a narrow E-W trending zone, ~400 km in length,
66 immediately north of the Periadriatic Lineament which is termed Eo-alpine high pressure belt (EHB)
67 (Hoinkes et al. 1991; Thöni and Jagoutz 1993; Exner et al. 2001; Sölva et al. 2005 a,b). The south-
68 easternmost part of the EHB is represented by eclogites of the Pohorje massif (e.g. Ippen 1892;
69 Hinterlechner-Ravnik and Moine 1977; Hinterlechner-Ravnik et al. 1991a,b; Janak et al. 2004; Miller
70 et al. 2005a; Vrabcic et al. 2012) and of the Koralpe and Saualpe basement complexes (Miller 1990;
71 Miller and Thöni 1997; Miller et al. 2005b) (Fig. 1a). Most Eoalpine eclogites including those from the
72 Pohorje massif are derived from MORB-type precursors (Miller et al. 1988; Miller and Thöni 1997;
73 Miller et al. 2005b) and only a minor part has intra-plate characteristics (Hoinkes et al. 1991; Konzett
74 et al. 2011). Major and trace element systematics of the Koralpe-Saualpe-Pohorje eclogites indicate
75 two different modes of formation of the precursors: (1) low-Mg gabbros derived from evolved tholeiitic
76 magmas not significantly influenced by cumulate formation and (2) high-Mg–Al–Ca gabbros depleted
77 in alkalis and with pronounced positive Eu-anomalies which are thought to represent plagioclase-rich
78 cumulates (Miller 1990; Sassi et al. 2004). A significant portion of these meta-cumulates contains
79 kyanite as a major constituent of the eclogite-facies assemblage (Sassi et al. 2004; Miller et al. 2005b,
80 2007).

81 Here we report the occurrence of high-Mg cumulate-type eclogites from the Pohorje Massif that
82 are unique amongst all eastern Alpine eclogites known so far in that their precursors contain Cr-spinel
83 as cumulate phase. These Cr-spinels create a geochemical micro-environment in which unusually Cr-
84 rich kyanite is present together with Cr-rich omphacite, pargasite and corundum. The Cr-contents of
85 kyanite are amongst the highest found so far in a natural environment. We present (1) mineral chemical
86 data for the Cr-rich high pressure assemblage along with bulk rock compositions of the host rocks, (2)

87 results of phase equilibrium calculations to determine *PT* conditions of formation of the Cr-rich phase
88 assemblage, and (3) a model for the formation of the Cr-rich phase assemblage

89

90

GEOLOGICAL SETTING

91 Eclogites and associated high-pressure metapelites form an important albeit small portion of the
92 Eastern alpine crystalline basement and testify to intracontinental subduction during Jurassic to
93 Cretaceous collision of the African and Eurasian lithospheres (Thöni 1999). Peak *PT*-conditions for the
94 Eoalpine eclogite-facies metamorphism increase from ~1.2 GPa and 550°C in the westernmost portions
95 of the Eastern Alps to ~3.0 GPa and 800°C in the Pohorje Massif (Hoinkes et al. 1991; Janak et al.
96 2004; Miller and Konzett 2005; Vrabec et al. 2012; this study). A multitude of geochronological
97 methods applied to the eclogite facies assemblages yields consistent ages of 85–115 Ma (Thöni 2006
98 and references; Konzett et al. 2011). For the Pohorje Massif the age of high-*P* metamorphism is tightly
99 constrained by U-Pb zircon and whole rock-garnet Sm-Nd ages for eclogites and their host metapelites
100 with 90.7±1.0 and 92.0±0.5 Ma, respectively (Miller et al. 2007; Janak et al. 2009). For the mainly
101 gabbroic eclogite precursors, Permian emplacement ages in the range 247–275 Ma were determined
102 (Thöni and Jagoutz 1993; Miller and Thöni 1997). In terms of large-scale tectonics the Pohorje Massif
103 is a nappe stack which consists of three tectonic units (Mioč and Žnidarčič 1977; Fodor et al. 2003)
104 (Fig. 1b). The lowermost unit is termed Pohorje nappe (Janák et al. 2006) and consists of medium to
105 high-grade micaschist, gneiss and amphibolite with lenses of marble, quartzite, eclogite and ultrabasic
106 rocks. This unit is folded into an ESE–WNW-striking antiform containing the Pohorje tonalite-
107 granodiorite in its core which was emplaced during the Oligocene to Miocene (Altherr et al. 1995;
108 Fodor et al. 2008). The Pohorje nappe is overlain by low-grade metamorphic Paleozoic slate and
109 phyllite and the uppermost nappe on top of these rocks consists of Permo-Triassic sandstone and
110 conglomerate. This nappe stack is covered by early Miocene sediments of the Pannonian Basin.

111 The eclogite samples investigated in this study were collected from poorly exposed outcrops
112 along a road situated at N 46° 24' 14.3" and E 015° 29' 25.7" close to Slovenska Bistrica (Fig. 1b).

113

114

ANALYTICAL METHODS

115 Mineral compositions were determined with a scanning electron microprobe JEOL JSM-6310 at the University of
116 Graz, Austria, using an energy and wavelength dispersive spectrometer (15 kV acceleration voltage and 6 nA beam current)
117 with 30 seconds on peak and 15 seconds on background for elements determined by WDX. The following standards were
118 used: Na (WDX), jadeite; Fe, Mg (EDX), garnet and kaersutite; K, Al, Si (EDX), adularia; Ca, Ti (EDX), titanite; Cr
119 (EDX), chromite; Mn (EDX), rhodonite; Zn (EDX), gahnite; F (WDX), synthetic F-phlogopite. Since Si content in phengite
120 is crucial for pressure determination, a muscovite standard was used instead of adularia for Si in order to ensure a similar
121 matrix for analyses of unknowns and standard. Additional electron microprobe analyses were obtained using a JEOL
122 Superprobe JXA 8200, Universitaetszentrum für Angewandte Geowissenschaften (UZAG) at the University of Leoben
123 (Austria). Analytical conditions were 15 kV accelerating voltage and 10 nA beam current with 30 seconds on peaks and 15
124 seconds on backgrounds of the X-ray lines. Zirconium in rutile was analyzed using a JEOL JXA-8100 Superprobe at the
125 University of Innsbruck with analytical conditions of 15 kV and 150 nA. Counting times were set to 300 sec on the peak
126 and 150 sec on the backgrounds of the ZrL α line using a PETH-crystal. This yields a 2-sigma count statistical error of 9%
127 for a Zr concentration of 300 ppm. The accuracy of Zr measurements was checked intermittently with a rutile standard
128 kindly supplied by T. Zack. Mineral formulae and single geothermobarometer reactions were calculated with the
129 Mathematica package PET (Dachs 2004).

130 Whole rock major and trace element compositions were determined by X-ray fluorescence spectroscopy using a
131 Bruker Pioneer S4 XRF at the Institute of Earth Sciences, University of Graz. The samples were prepared as fused pellets
132 using 7 gram of Li₂B₄O₇ and 1 gram of finely powdered and dried sample. The loss on ignition (LOI) was determined from
133 the total weight change after heating to 1030°C for 1 hour.

134 Unpolarized spectra of kyanites were measured on a HORIBA Labram HR-800 confocal Raman-spectrometer,
135 using the 514 nm excitation wavelength of a 30 mW Nd-YAG laser, through a 100x objective with a numerical aperture of
136 0.9. Standard optical and electron microprobe backscattered electron images were used to target areas that are homogeneous
137 in composition and free of visible inclusions. Size and power of the laser spot on the surface was approximately 1 μ m and 5

138 mW, respectively. Confocal pinhole and entrance slit were set to 1000 and 100 μm . The scattered Raman light was
139 dispersed by a grating with 1800 lines/mm and detected by an open-electrode CCD with 1024 x 256 pixels, each sizing 43
140 μm . The spectral resolution, determined by measuring the Rayleigh line, was 1.4 cm^{-1} . Background and Raman bands were
141 fitted by the built-in spectrometer software LabSpec to first or second order polynomials and convoluted Gauss-Lorentz
142 functions. The accuracy of Raman line shifts was checked by regular measurements of the emission lines of a Ne spectral
143 calibration lamp and is on the order of 0.5 wavenumbers.

144

145 **WHOLE ROCK GEOCHEMISTRY AND SAMPLE PETROGRAPHY**

146 The samples contain 43.3–49.9 wt% SiO_2 along with 13.6–22.9 wt% Al_2O_3 , 11.8–18.5 wt%
147 CaO and 9.1–14.7 wt% MgO. Mg-numbers [$100 \cdot \text{Mg}/(\text{Mg}+\text{Fe})$] are between 75 and 91. Na_2O shows a
148 variation of 1.4–3.1 wt%, Cr and Ni contents are 476–4908 ppm and 166–469 ppm, respectively, with
149 the Cr-spinel bearing samples PM22 and PM26 showing the highest Cr and Ni contents of any
150 eclogites reported so far from the Pohorje Massif (Sassi et al. 2004; Miller et al. 2007). In the Al_2O_3 –
151 TiO_2 diagram devised by Pearce (1983) all but two samples plot into the field for plagioclase-rich
152 cumulates (Fig. 2a) which is consistent with high Mg-numbers and CaO contents and with the
153 extremely low K_2O and P_2O_5 contents. The positive correlation trends in X_{mg} versus Cr, Ni, Al_2O_3 ,
154 CaO are similar albeit with a larger scatter compared to those reported by Sassi et al. (2004) and Miller
155 et al. (2007) for cumulate-type (high-Mg) eclogites (Figs. 2b-e) from other localities of the Pohorje
156 Massif.

157 All investigated eclogites show either equigranular, or in rare instances, corona textures with a
158 mm-scale grain size and characterized by the assemblage omphacite+garnet+rutile. Kyanite, calcic
159 amphibole, zoisite, quartz and accessory phase zircon are common in most samples while phengite and
160 corundum are rarely present. The Cr-spinel bearing samples PM22 and PM26 contain
161 omphacite+garnet+kyanite+calcic amphibole+phengite+quartz+rutile+zircon and

162 omphacite+garnet+calcic amphibole+kyanite+zoisite+corundum, respectively (Figs. 3a,b). Both, PM22
163 and PM26, show variable degrees of retrogression evidenced by extremely fine-grained symplectites
164 around omphacite, garnet, kyanite, phengite, and calcic amphibole.

165 Matrix omphacite forms anhedral to subhedral grains which appear unaffected by retrogression
166 or, more commonly, are mantled by plagioclase±calcic amphibole±clinopyroxene symplectites (symp
167 I) (Fig. 4a). The textures of the omphacite-symplectites indicate a two stage growth commencing with
168 the formation of clinopyroxene+plagioclase followed by calcic amphibole growth at the expense of the
169 former two phases. Omphacite is also present as well preserved inclusions in large matrix kyanite even
170 when matrix omphacite was completely retrogressed and as rare constituent of reaction coronas around
171 Cr-spinel.

172 Garnet forms rounded grains with inclusions of kyanite and/or omphacite and are often partially
173 replaced by calcic amphibole±plagioclase symplectites (symp II) (Fig. 4a,b). Sometimes chlorite is part
174 of the garnet-symplectites and partially replaces calcic amphibole.

175 Kyanite is present as large euhedral crystals up to several hundred μm in size either as a matrix
176 phase or as tiny ($\leq 10 \mu\text{m}$) needles included in garnet. In sample PM22 matrix kyanite sometimes
177 contains clusters of small ($< 50\text{-}100 \mu\text{m}$) drop-like Cr-spinel inclusions in part intergrown with rutile
178 and omphacite (Fig. 3a). Around these spinel inclusions the kyanite shows a strikingly blue to turquoise
179 color and an intense deep-blue–light blue pleochroism. A second textural type of kyanite only occurs as
180 part of Al-rich reaction coronas around large ($\leq 1 \text{ mm}$) Cr-spinel matrix grains in sample PM26 (Fig.
181 3b). The kyanite, too, shows deep blue color and forms needle-like crystals intergrown with chromian
182 Al-rich pargasite and Cr-rich corundum. Matrix kyanite often displays variable degrees of retrogressive
183 replacement by extremely fine-grained symplectite rims (symp III). BSE-imaging reveals a two layer
184 structure with an inner layer immediately adjacent to kyanite consisting of intermediate plagioclase
185 (An_{50})+corundum+spinel±sapphirine and an outer layer of calcium-richer plagioclase (An_{90})±calcic

186 amphibole directed towards the eclogite matrix phases (Fig. 4c). Both corundum and spinel are close to
187 endmember Al_2O_3 and MgAl_2O_4 , respectively and sapphirine is strongly peraluminous.

188 Phengite was only found in PM22 as rare lath-shaped crystals of up to 300 μm in length which
189 are partially replaced by biotite+plagioclase symplectites (symp IV) (Figs. 4d,e).

190 Two textural types of amphibole are present in the samples investigated. Texturally primary
191 amphibole forms large subhedral and almost colorless grains scattered in the matrix which are in
192 textural equilibrium with omphacite, garnet and kyanite. This amphibole develops, in some instances,
193 thin symplectitic rims (symp V) (Fig. 4d). Texturally secondary amphibole is present as reaction rims
194 around garnet and as part of Al-rich reaction coronas around Cr-spinel matrix grains as found in sample
195 PM26 (Fig. 4f). Secondary amphibole which is part of the Al-rich reaction coronas do not exceed ~ 300
196 μm in size and, if sufficiently rich in Cr, may show a pronounced lime green color and green-to-
197 colorless pleochroism (Fig. 3b).

198 Corundum is present in three textural types: corundum-I is a matrix phase and forms euhedral
199 colorless crystals of up to 300 μm in size in textural equilibrium with garnet, omphacite and calcic
200 amphibole. It often contains inclusions of kyanite and omphacite (Fig. 4f). Corundum-II forms
201 vermicular grains as part of symplectites around kyanite (Fig. 4c) and corundum-III is exclusively
202 present in Cr-spinel reaction coronas intergrown with chromian Al-rich pargasite and Cr-kyanite and
203 shows an intensely red to pink color and strong pleochroism (Fig. 4f).

204 Cr-spinel was found in PM22 as clusters of honey yellow droplets $< 50\text{-}100$ μm in size included
205 in matrix kyanite (Fig. 3a) and in PM26 as reddish-brown euhedral and often strongly poikilitic crystals
206 of up to 1 mm in size. Cr-spinel in PM26 always possesses a spectacular two-layer reaction corona
207 which consists of an inner layer of blue kyanite needles intergrown with pink corundum-III and an
208 outer layer of light green pargasite (Fig. 3b).

209 Additional minor to accessory constituents of the eclogite-facies assemblages from sample

210 PM26 is zoisite and pentlandite. PM22 contains zircon and rutile with rutile forming small drop-like
211 inclusions in kyanite associated with Cr-spinel or occurring as matrix phase. Zoisite is present in sample
212 PM26 only as small matrix grains intergrown with omphacite, garnet and/or kyanite.

213

214 MINERAL CHEMISTRY

215 Garnet is pyrope-rich with an observed compositional range pyrope₄₉₋₅₃grossular₁₉₋
216 ₂₀almandine₂₇₋₃₁spessartite_{0.5-2} in PM22 and pyrope₆₀₋₆₈grossular₂₁₋₂₅almandine₁₁₋₁₄spessartite_{<1} in
217 PM26, respectively (Figs. 4a,b; Tables 1, 2). No significant compositional zoning could be observed in
218 any of the garnets analyzed. The garnet composition mainly reflects differences in the whole rock
219 composition of the two samples as evidenced by garnet X_{Mg} [$=Mg/(Mg+Fe^{2+})$] of 0.61-0.66 in PM22
220 and of 0.81-0.86 in the unusually Mg-rich cumulate PM26. (Table 2).

221 Matrix omphacite and omphacite inclusions in kyanite are typically unzoned with an observed
222 compositional range diopside₅₆₋₅₉jadeite₃₁₋₃₄calcium Tschermak's pyroxene_{0.03-0.04}acmite_{0.00-0.03} in
223 PM22 and diopside₅₇₋₆₃jadeite₂₇₋₂₉calcium Tschermak's pyroxene_{0.05-0.08}acmite_{<0.01} in PM26,
224 respectively (Tables 1, 2). Aside from large Cr-poor matrix omphacite, Cr-rich omphacite is present in
225 sample PM26 as part of a reaction corona around large Cr-spinel grains and in sample PM22 associated
226 with Cr-spinel droplets as inclusions in kyanite. This omphacite contains as much as 5.3 wt% Cr₂O₃,
227 equivalent to 14.8 mol% NaCrSi₂O₆ (kosmochlor) component (Table 3).

228 Large matrix kyanite crystals devoid of Cr-spinel inclusions are homogeneous and show a
229 close-to-endmember composition. Kyanite with clusters of drop-like Cr-spinel inclusions from sample
230 PM22 shows a strong and complex discontinuous Cr-zoning in the vicinity of Cr-spinel (Fig. 5) with
231 highly variable Cr₂O₃ contents reaching 15.6 wt% which is equivalent to 17.6 mol% X_{Cr-Ky} (Table 4;
232 Fig. 6). Fe₂O₃ contents of the Cr-rich zones reach 0.6 wt% and are positively correlated with Cr₂O₃
233 contents. Cr-rich kyanite in reaction coronas around Cr-spinels from sample PM26 does not display

234 any Cr-zoning and shows lower Cr₂O₃ contents not exceeding 8.2 wt%. In order to test the effect of Cr–
235 Al exchange on the Raman spectra of kyanite, five compositionally homogeneous areas of sufficient
236 size within zoned Cr-bearing kyanites containing 0.6, 2.1, 6.1, 8.9, and 10.7 wt% Cr₂O₃ were selected
237 and Raman spectra recorded. Increasing Cr contents result in a systematic and linear shift of the major
238 bands towards lower wave numbers accompanied by a broadening of the bands (Fig. 7a). For example
239 the band at 487 cm⁻¹ in the spectrum of kyanite with 0.6 wt% Cr₂O₃ is shifted to 481 cm⁻¹ in the
240 spectrum of kyanite with 10.7 wt% Cr₂O₃. The corresponding increase in band width at half height is
241 from 4.4 to 12.2 cm⁻¹ (Fig. 7b).

242 Matrix corundum-I only shows very minor Al substitution by Cr and Fe³⁺ (Table 2) whereas
243 corundum-II within symplectites around kyanite is pure Al₂O₃. By contrast, corundum-III is
244 characterized by variable and in part extremely high Cr₂O₃ contents of up to 9.1 wt% which
245 corresponds to an eskolaite component of up to 6.3 mol.% (Table 4).

246 Spinel from sample PM22 is Cr-Fe-dominated and contains minor Al, Mg and Zn (Table 4). In
247 terms of endmembers, the observed range in composition is chromite₅₅₋₅₆magnesio-chromite₂₂₋
248 ₂₄magnetite₀₁₋₀₄hercynite₁₄₋₁₅gahnite₀₃₋₀₄. In sample PM26 spinel shows significantly lower Fe and Cr
249 combined with higher Al and Mg contents. The observed range in composition is chromite₀₀₋
250 ₀₅magnesiochromite₅₁₋₅₆magnetite₀₁₋₀₂hercynite₁₄₋₁₅gahnite₀₁₋₀₂spinel₀₀₋₁₄. (Fig. 8).

251 Texturally primary amphibole is barroisite to magnesio-hornblende (Leake et al. 2004) (Fig. 9)
252 which contains minor K, Ti and Cr (Tables 1, 2). The texturally secondary amphibole present in the Al-
253 rich spinel reaction coronas in sample PM26 is pargasite, alumino-pargasite or chromian pargasite
254 (Table 3). Cr₂O₃ contents are highly variable with 0.1-3.9 wt% and decrease with increasing distance
255 from Cr-spinel. The positive Cr-^[IV]Al and negative Cr-^[VI]Al correlations are consistent with a
256 combined Tschermaks and ^[VI]Al=^[VI]Cr exchange.

257 Phengite from sample PM22 shows 3.25-3.35 Si a.p.f.u. along with minor paragonite solid-

258 solution [(Na/(K+Na+Ca))= 0.04-0.07] (Table 1).

259 Matrix rutile contains 0.2-0.8 wt% Cr₂O₃ and 0.3-0.4 wt% Fe₂O₃ along with 302-403 ppm Zr
260 and <65 ppm Nb (n=9). The rutile inclusions in kyanite associated with Cr-spinel-I show significantly
261 higher Cr₂O₃ (1.5-1.9 wt%) and Nb (206-289 ppm) combined with lower Fe₂O₃ (0.05-0.13 wt%) and
262 Zr (194-330 ppm) (Table 5).

263

264 ***PT* CONDITIONS OF ECLOGITE FACIES METAMORPHISM**

265 **Phase equilibrium calculations**

266 Estimates of *PT* conditions of eclogite-facies metamorphism in the Pohorje eclogites are
267 controversial. Janak et al. (2004) and Vrabec et al. (2012) reported conditions of ~820°C and 3 GPa
268 based on the garnet-omphacite-phengite thermobarometer from Krogh-Ravna and Terry (2004).
269 Results of Sassi et al. (2004), Miller et al. (2005a) and Miller and Konzett (2005) yield consistently
270 lower *PT* estimates of 650–720°C and 2.1–2.6 GPa. Sample PM22 contains the assemblage
271 garnet+omphacite+phengite which allows the application of various geothermobarometers. Using
272 different thermodynamic datasets and activity models but the same mineral compositions, *PT*
273 conditions in the range 640-810°C and 2.0–2.9 GPa were obtained using reactions (1) – (3) or reactions
274 (1) and (4) (Table 1, Fig. 10).

275



280

281 The highest *PT* values of 780–810°C at 2.7-2.9 GPa were calculated using the net transfer reactions

282 (1)–(3) which are considered robust because they are independent of ferric/ferrous iron consideration
283 using the calibration of Krogh-Ravna and Terry (2004). Using the thermodynamic database from
284 Holland and Powell (1998) and calculating activities with AX_2
285 (<http://www.esc.cam.ac.uk/research/research-groups/research-projects/tim-hollands-software-pages/ax>)
286 reactions (1)–(3) yield significantly lower *P* conditions of 2.0–2.1 GPa at a similar *T* of 770–780°C.
287 The calibration of Brandelik and Massonne (2004) for reactions (1)–(3) yields 710–760°C at 2.4–2.5
288 GPa. The lowest temperatures of 640–680°C and intermediate pressures of 2.2–2.3 GPa are obtained
289 using clinopyroxene-garnet Fe²⁺–Mg exchange thermometry (reaction 4, Krogh, 2000) together with an
290 updated version of the Waters and Martin (1993) garnet-clinopyroxene-phengite barometer (reaction
291 1).

292 To provide additional constraints on temperatures of equilibration for the Cr-kyanite bearing
293 assemblages, Zr-in-rutile thermometry was applied to sample PM22 in which rutile is present as small
294 (≤40x70 μm) inclusions in Cr-kyanite associated with Cr-spinel and also as larger (≤350x450 μm)
295 grains scattered in the matrix. Although individual rutile grains are compositionally unzoned within the
296 analytical error of an individual analysis, there is some inter-grain variation (Table 5). Using a pressure
297 of 2.5 GPa, averaged temperatures derived from 14 rutile analyses are 721±25°C and 717±17°C based
298 on the calibrations devised by Zack et al. (2004) and Thomkins et al. (2007), respectively. Averaged
299 temperatures for rutile inclusions in Cr-kyanite and for matrix grains do not yield statistically different
300 values.

301

302

DISCUSSION

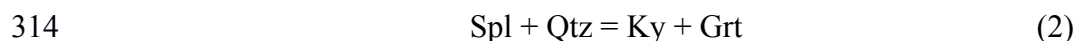
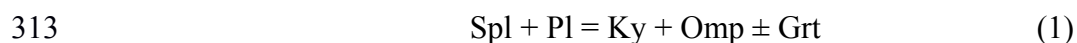
303 **The formation of Cr-kyanite in the context of high-P metamorphism in the Pohorje Massif**

304 In samples PM22 and PM26 Cr-kyanite occurs in two different textures, namely (1) as matrix

305 kyanite with \pm irregularly shaped Cr-rich segments around Cr-spinel inclusions and (2) as part of
306 reaction coronas around large Cr-spinel grains.

307 In case of PM22 it is obvious that Cr-spinel was consumed while matrix kyanite formed (Figs.
308 3,5). Because the Cr-rich kyanite portions are part of the large matrix kyanites we suggest that this
309 reaction took place during prograde metamorphism. Omphacite and rutile inclusions are also found
310 together with Cr-spinel in the Cr-rich kyanites. Possible simplified endmember reactions involving
311 spinel as a reactant phase are:

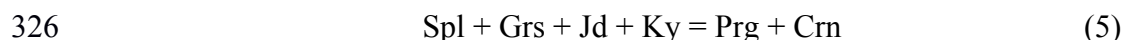
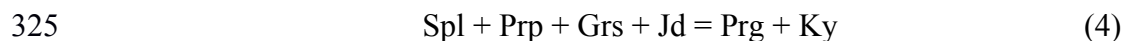
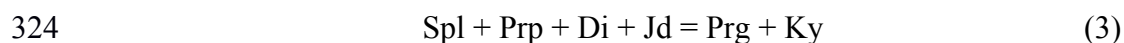
312



315

316 Unlike in sample PM22, the large Cr-spinels in sample PM26 did not break down during a
317 significant portion of the prograde metamorphic *PT* path. Textures clearly indicate that Cr-spinel reacts
318 with omphacite and garnet to produce a spherical corona consisting of an inner portion that contains
319 Cr-rich kyanite and an outer portion mainly consisting of chromian pargasite (Fig. 3b). Cr-rich
320 corundum as well as omphacite occur in subordinate amounts mainly in the inner portions of the
321 coronas. Based on the observed mineral assemblages in PM26, potential kyanite and corundum
322 producing reactions are

323



327

328 Their location in *PT* space was calculated in NCMASH system using appropriate activity models (Fig.

329 [11a](#)). Following a decompression PT path, crystallization of Cr-rich kyanite occurs at significantly
330 higher pressures than formation of Cr-rich corundum. However, a change in water activity may shift
331 reactions to lower T and P . Nevertheless, textural evidence does not support this conclusion that these
332 minerals formed at different stages along the retrograde path.

333 In general, corona textures indicate that a mineral reaction did not proceed to completion and
334 are a sign of disequilibrium. In case of samples PM22 and PM26, Cr-spinel is a magmatic relic inherited
335 from the eclogite precursor rock and started to react with the eclogite facies minerals garnet and
336 omphacite during progressive metamorphism. As evidenced by the presence of abundant pargasite
337 within the reaction coronas, hydrous fluids must have been involved in the corona formation. These
338 fluids are rarely pure H_2O but usually contain variable amounts of CO_2 along with various dissolved
339 species amongst which $SiO_{2,aq}$ and $NaCl_{aq}$ are often dominant (e.g. Hauzenberger et al., 2001;
340 Manning, 2004). An influx of hydrous fluid associated with a change in the chemical potential of SiO_2
341 and/or Na_2O at the interface between Cr-spinel and the matrix phases provides a potential explanation
342 for corona formation as outlined in [Fig. 11b](#) which shows a SiO_2 versus Na_2O chemical potential
343 diagram for $800^\circ C$ and 2.5 GPa that was calculated using the activity models as for [Fig. 11a](#). [Figure](#)
344 [11b](#) shows that at pressures and temperatures close to the peak of Eoalpine eclogite-facies
345 metamorphism and in a chemical system characterized by $a_{SiO_2} < 1$, an increase in μ_{SiO_2} resulting from
346 an influx of fluid may trigger pargasite and/or kyanite-formation through the following reactions ([Fig.](#)
347 [11b](#)):



352

353 The chemical potential of Na_2O probably did not change significantly during reaction progress because
354 of abundant omphacite present in the matrix that buffers this component.

355

356 **The timing of Cr-kyanite formation**

357 Green and Ringwood (1967) showed that phases with aluminium-rich compositions form
358 kyanite in eclogites with the breakdown of plagioclase occurring at approximately 1.5 GPa and 700°C.
359 Cr-spinel overgrown by and eventually enclosed in newly formed but still Cr-poor kyanite is thought to
360 represent the first step in the formation of Cr-kyanites in sample PM22 that took place at pressures
361 above approximately 1.5 GPa. In a second step rising P and T caused increasing Cr_2SiO_5 -solubility in
362 kyanite resulting in an exchange reaction $\text{Al}_2\text{SiO}_5 + \text{FeCr}_2\text{O}_4 = \text{Cr}_2\text{SiO}_5 + \text{FeAl}_2\text{O}_4$ involving newly
363 formed kyanite and Cr-spinel inherited from the magmatic precursor (cf. Gil-Ibarguchi et al. 1991).
364 Thus, Cr-kyanite from sample PM22 predates the formation of Cr-rich corona kyanite from sample
365 PM26 whose formation requires the breakdown of eclogite-facies phases during the retrograde portion
366 of the PT -path.

367 Retrogression of eclogite to amphibolite is widespread in the Saualpe, Koralpe and Pohorje area
368 of the Eastern Alpine basement and is attributed to a pervasive fluid influx during uplift. Based on the
369 fluid-influx model as outlined in [Fig. 11b](#) the formation of Cr-rich kyanites within the spinel coronas
370 from sample PM26 is not a prograde but a retrograde phenomenon associated with the earliest stage of
371 the exhumation path but under still high pressures. This is supported by small inclusions of Cr-rich
372 omphacite found within the coronas which are a clear indication for eclogite facies conditions. Hence,
373 mineral textures and phase equilibrium calculations would be consistent with the following scenario
374 ([Fig. 12](#)): during prograde metamorphism large magmatic Cr-spinel grains initially remained
375 unaffected by rising PT conditions due to sluggish reaction kinetics. Influx of a hydrous fluid during
376 the initial stage of decompression increased the chemical potential of SiO_2 and strongly accelerated

377 reaction kinetics, allowing various kyanite-, amphibole-, and corundum-forming reactions to proceed.
378 The spatial distribution of phases within the coronas is consistent with increasing chemical potential of
379 SiO₂ and decreasing chemical potentials of Al₂O₃ and Cr₂O₃ from spinel towards the matrix (Fig. 12).

380

381

IMPLICATIONS

382 Within the two investigated samples PM22 and PM26, Cr-spinel-bearing gabbroic cumulates
383 from the Pohorje Massif, blue Cr-kyanite formed in two different textural micro-environments. A first
384 type present in sample PM22 encloses clusters of small drop-like Cr-spinel inclusions and contains up
385 to 15.6 wt% Cr₂O₃. The most intense blue color occurs in the immediate vicinity to the Cr-spinel. A
386 second type is present in sample PM26 as part of Al-rich reaction coronas developed around large red-
387 brownish Cr-spinel magmatic relics. Within these coronas Cr-kyanite appears as deep blue needle-like
388 crystals that contain up to 8.2 wt% Cr₂O₃ and is associated with red-pink Cr-rich corundum containing
389 up to 9.1 wt% Cr₂O₃ and Cr-Al-rich pargasite with up to 3.9 wt% Cr₂O₃. The blue color of kyanite and
390 the red-pink color of corundum are a result of Cr-Al substitution in octahedral sites during high
391 pressure/ultra-high pressure metamorphism. Whereas Cr-kyanite in sample PM22 formed under
392 increasing *PT* conditions during prograde metamorphism, Cr-kyanite and the associated Cr-rich
393 corona-assemblage in sample PM26 were generated during the earliest stage of retrogressive evolution
394 of these rocks still at eclogite-facies *PT* conditions of ~2.5 GPa and 750-800°C.

395

396

ACKNOWLEDGMENTS

397 We would like to thank Zmargo Zorg, Anton Gutschi and Walter Postl for their support during field
398 work. We are particularly indebted to Zmargo Zorg who has been ranging the Pohorje Massif for
399 eclogite occurrences for many years. Anton Pock, Juergen Neubauer, Karl Ettinger, and Reinhard
400 Kaindl are thanked for thin section preparation, SEM support, performing EPMA analysis, and support

401 for Raman analysis, respectively. We thank Håkon Austrheim, Gerhard Franz and an unknown
402 reviewer for their comments and corrections.

403

404

405

REFERENCES CITED

406

407 Altherr, R., Lugovic, B., Meyer, H.P., and Majer, V. (1995) Early Miocene post-collisional calc-
408 alkaline-magmatism along the easternmost segment of the periadriatic fault system (Slovenia and
409 Croatia). *Mineralogy and Petrology* 54, 225-247.

410 Brandelik, A., and Massonne, H.J. (2004) PTGIBBS - an EXCEL™ Visual Basic program for
411 computing and visualizing thermodynamic functions and equilibria of rock-forming minerals.
412 *Computers and Geosciences*. 30, 909-923.

413 Chinner G.A., Smith J.V., and Knowles C.R. (1969) Transition metal contents of Al₂SiO₅ polymorphs.
414 *American Journal of Science*, 267-A, 96–113.

415 Connolly, J.A.D. (1990) Multivariable phase-diagrams - an algorithm based on generalized
416 thermodynamics. *American Journal of Science* 290, 666-718.

417 Cooper, A.F. (1980) Retrograde alteration of chromian kyanite in metachert and amphibolite
418 whiteschist from the Southern Alps, New Zealand, with implications for uplift on the Alpine
419 Fault. *Contributions to Mineralogy and Petrology* 75, 153-164.

420 Dachs, E. (2004) PET: petrological elementary tools for Mathematica: an update. *Computers and*
421 *Geosciences*, 30, 173–182.

422 Delor, C.P., and Leyreloup, A.F. (1986) Chromium-rich kyanite in an eclogite from the Rouergue area,

- 423 French Massif Central. Mineralogical Magazine 50, 535-537.
- 424 Exner, U., Füsseis, F., Grasemann, B., Habler, G., Linner, M., Sölva, H., Thiede, R., Thöni, M., (2001)
425 Cretaceous Eclogite-Facies Metamorphism in the Eastern Alps: new insights, data and
426 correlations from an interdisciplinary study. Journal of Conference Abstracts (Abstract volume
427 EUG XI) 6, 387.
- 428 Ferry, J.M. and Watson, E.B. (2007) New thermodynamic models and revised calibrations for the Ti-
429 in-zircon and Zr-in-rutile thermometers. Contributions to Mineralogy and Petrology 154, 429-437
- 430 Fodor, L.I., Balogh, K., and Dunkl, I. (2003) Structural evolution and exhumation of the Pohorje-
431 Kozjak Mts., Slovenia. Ann. Univ. Scient. Budapest. Sect. Geol. 35, 118-119.
- 432 Fodor, L.I., Gerdes, A., Dunkl, I., and Koroknai, B. (2008) Miocene emplacement and rapid cooling of
433 the Pohorje pluton at the Alpine-Pannonian-Dinaridic junction, Slovenia. Swiss Journal of
434 Geosciences, doi:10.1007/s00015-008-1286-9.
- 435 Gil-Ibarguchi, J.I., Mendia, M., and Girardeau, J. (1991) Cr-rich staurolite and Cr-rich kyanite in high-
436 pressure ultrabasic rocks (Cabo Ortegal, northwestern Spain) American Mineralogist 76, 501-
437 511.
- 438 Grambling, J.A., and Williams, M.L. (1984). The Effects of Fe³⁺ and Mn³⁺ on Aluminum Silicate
439 Phase Relations in North-Central New Mexico, U.S.A. Journal of Petrology, 26, 324-354.
- 440 Green, D.H., and Ringwood, A.E. (1967) An experimental investigation of the gabbro to eclogite
441 transformation and its petrological applications. Geochimica et Cosmochimica Acta, 31, 767-833.
- 442 Hauzenberger, C.A., Baumgartner, L.P., and Pak T.M. (2001). Experimental Study on the Solubility of
443 the "Model"-Pelite Mineral Assemblage Albite + K-Feldspar + Andalusite + Quartz in
444 Supercritical Chloride Rich Aqueous Solutions at 0.2 GPa and 600°C, Geochimica et

- 445 Cosmochimica Acta, 65, 4493-4507.
- 446 Hinterlechner-Ravnik, A., and Moine, B. (1977) Geochemical characteristics of the metamorphic rocks
447 of the Pohorje Mountains. Geologija, 20, 107-140.
- 448 Hinterlechner-Ravnik, A., Sassi, F.P., and Visona, D., (1991a) The Austridic eclogites, metabasites and
449 metaultrabasites from the Pohorje area (Eastern Alps, Yugoslavia): 1. The eclogites and related
450 rocks. Rend.Fis.Accad.Lincei, 2, 157-173.
- 451 Hinterlechner-Ravnik, A., Sassi, F.P., and Visona, D. (1991b) The Austridic eclogites, metabasites and
452 metaultrabasites from the Pohorje area (Eastern Alps, Yugoslavia): 2. The metabasites and
453 metaultrabasites, and concluding considerations. Rend.Fis.Accad.Lincei, 2, 175-190.
- 454 Hoinkes, G., Kostner, A., and Thöni, M. (1991) Petrologic constraints for the Eo-alpine eclogite facies
455 metamorphism in the Austro-Alpine basement. Mineralogy and Petrology, 43, 237-354.
- 456 Holland, T.J.B., and Powell, R. (1998) An internally consistent thermodynamic data set for phases of
457 petrological interest. Journal of Metamorphic Geology, 16, 309–343.
- 458 Holland, T.J.B., 1990. Activities of components in omphacitic solid solutions. An application of
459 Landau theory to mixtures. Contributions to Mineralogy and Petrology, 105, 446-453.
- 460
- 461 Ippen, J.A. 1892 Zur Kenntnis der Eklogite und Amphibolite des Bachergebirges. Mitteilungen des
462 Naturwissenschaftlichen Vereins für Steiermark, 328-369.
- 463 Janák, M., Froitzheim, N., Lupták, B., Vrabec, M., and Krogh Ravná, E.J. (2004) First evidence for
464 ultrahigh-pressure metamorphism of eclogites in Pohorje, Slovenia: Tracing deep continental
465 subduction in the Eastern Alps. Tectonics, 23, TC5014, doi:10.1029/2004TC001641.

- 466 Janák, M., Froitzheim, N., Vrabec, M., Krogh Ravná, E.J., and de Hoog, J.C.M. (2006)
467 Ultrahighpressure metamorphism and exhumation of garnet peridotite in Pohorje, Eastern Alps.
468 *Journal of Metamorphic Geology*, 24/1, 19-31.
- 469 Janák, M., Cornell, D., Froitzheim, N., De Hoog, J.C.M., Broska, I., and Vrabec, M. (2009) Eclogite-
470 hosting metapelites from the Pohorje Mountains (Eastern Alps): P-T evolution, zircon
471 geochronology and tectonic implications. *European Journal of Mineralogy*, 21, 1191-1212.
- 472 Konzett, J., Krenn, K., Hauzenberger, Ch., Whitehouse, M., and Hoinkes, G. (2011). High-pressure
473 tourmaline formation and fluid activity in Fe–Ti-rich eclogites from the Kreuzeck Mountains,
474 Eastern Alps, Austria. *Journal of Petrology*, doi: 10.1093/petrology/egr057.
- 475 Krogh, E.J. (2000) The garnet-clinopyroxene Fe²⁺-Mg geothermometer: an updated calibration. *Journal*
476 *of Metamorphic Geology*, 18, 211-219.
- 477 Krogh-Ravná, E.J., and Terry, P. (2004) Geothermobarometry of UHP and HP eclogites and schists -
478 an evaluation of equilibria among garnet-clinopyroxene-kyanite-phengite-coesite/quartz. *Journal*
479 *of Metamorphic Geology*, 22:579-592.
- 480 Langer, K., and Seifert, F. (1974) High pressure-high temperature synthesis and properties of chromian
481 kyanite, (Al,Cr)₂SiO₅. *Zeitschrift für anorganische und allgemeine Chemie*, 383, 29-39.
- 482 Manning, C.E. (2004) The chemistry of subduction-zone fluids. *Earth and Planetary Science Letters*,
483 223, 1–16.
- 484 Miller, C. (1990) Petrology of the type locality eclogites from the Koralpe and Saualpe (Eastern Alps),
485 Austria. *Schweizerische Mineralogische und Petrographische Mitteilungen*, 70, 287-300.
- 486 Miller, C., Stosch, H.G., and Hoernes, S. (1988) Geochemistry and origin of eclogites from the type
487 locality Koralpe and Saualpe, Eastern Alps, Austria. *Chemical Geology*, 67, 103-118.

- 488 Miller, C., and Thöni, M. (1997) Eo-Alpine eclogitisation of Permian MORB-type gabbros in the
489 Koralpe (Austria): new petrological, geochemical and geochronological data. *Chemical Geology*,
490 137, 283-310.
- 491 Miller, C., and Konzett, J. (2005a) Comment on First evidence for Ultrahigh pressure metamorphism of
492 eclogites in Pohorje, Slovenia: tracing deep continental subduction in the eastern Alps by Janák et
493 al. (2004). *Tectonics* 24:TC6010. doi:10.1029/2004TC001765.
- 494 Miller, C., Mundil, R., Thöni, M., and Konzett, J. (2005b) Refining the timing of eclogite
495 metamorphism: a geochemical, petrological, Sm-Nd and U-Pb case study from the Pohorje
496 Mountains, Slovenia (Eastern Alps). *Contributions to Mineralogy and Petrology*, 150, 70-84.
- 497 Miller, C., Thöni, M., Konzett, J., Kurz, W., and Schuster, R. (2005) Eclogites from the Koralpe and
498 Saualpe type-localities, Eastern Alps, Austria. *Mitteilungen Österreichische Mineralogische*
499 *Gesellschaft*, 150, 227-263.
- 500 Miller, C., Zanetti, A., Thöni, M., and Konzett, J. (2007) Eclogitisation of gabbroic rocks:
501 redistribution of trace elements and Zr in rutile thermometry in an Eo-alpine subduction zone
502 (Eastern Alps). *Chemical Geology*, 239:96-123.
- 503 Mioč, P., and Žnidarčič, M. (1977) Geological Map of SFRJ. Geological Survey, Ljubljana, Slovenia.
- 504 Negulescu, E., and Sabau, G. (2012) Chromium-rich lawsonite in high-Cr eclogites from the Fagaras
505 Massif (South Carpathians). American Geophysical Union Fall Meeting poster V23D-2862
506 available under <http://www.igr.ro/proiecte/archimedes/docs/12SF2012.pdf>.
- 507 Pearce, J. A. (1983) A „user's guide“ to basalt discrimination diagrams. The Open University Report
508 (unpublished).
- 509 Pivin, M., Berger, J., and Demaiffe, D. (2011) Nature and origin of an exceptionally Cr-rich kyanite-

- 510 bearing xenolith from Mbuji-Mayi kimberlite (DRC) *European Journal of Mineralogy* 23, 257-
511 268.
- 512 Rost, F. and Simon, E. (1972) Zur Geochemie und Färbung des Cyanits. *Neues Jahrbuch für*
513 *Mineralogie Monatshefte* 9, 383-395.
- 514 Sassi, R., Mazzoli, C., Miller, C., and Konzett, J. (2004) Geochemistry and metamorphic evolution of
515 the Pohorje Mountain eclogites from the easternmost Austroalpine basement of the Eastern Alps
516 (Northern Slovenia). *Lithos*, 78, 235-261.
- 517 Sobolev, N.V., Kusnetsova, I.K., and Zyuzin, N.I. (1968) The petrology of grosspydite xenoliths from
518 the Zagadochnaya pipe in Yakutia. *Journal of Petrology* 9, 253-280.
- 519 Sölva, H., Grasmann, B., Thöni, M., Thiede, R.C., and Habler, G., (2005a) The Schneeberg Normal
520 Fault Zone: Normal faulting associated with Cretaceous SE-directed extrusion in the Eastern
521 Alps (Italy/Austria). *Tectonophysics*, 401, 143-166.
- 522 Sölva, H., Grasmann, B., Thöni, M., and Habler, G., (2005b) The eo-Alpine high-pressure belt in the
523 Eastern Alps: a kinematic exhumation model and its tectonic implications. *Mitteilungen*
524 *Österreichische Mineralogische Gesellschaft*, 150-147.
- 525 Thomkins, H.S., Powell, R. and Ellis, D.J. (2007) The pressure dependence of the zirconium-in-rutile
526 thermometer. *Journal of Metamorphic Geology* 25, 703-713.
- 527 Thöni, M., and Jagoutz, E. (1993) Isotopic constraints for Eo-Alpine high-P metamorphism in the
528 Austroalpine nappes of the Eastern Alps: bearing on Alpine orogenesis. *Schweizerische*
529 *Mineralogische und Petrographische Mitteilungen*, 73, 177-189.
- 530 Thöni, M. (1999) A review of geochronological data from the Eastern Alps. *Schweizer Mineralogisch*
531 *Petrographische Mitteilungen*, 79, 209–230.

- 532 Thöni, M. (2006) Dating eclogite facies metamorphism in the Eastern Alps-approaches, results,
533 interpretations: a review. *Mineralogy and Petrology*, 88, 123-148.
- 534 Vrabc, M., Janák, M., Froitzheim, N., and De Hoog, C.-J. (2012) Phase relations during peak
535 metamorphism and decompression of the UHP kyanite eclogites, Pohorje Mountains (Eastern
536 Alps, Slovenia). *Lithos*, 144–145, 40-55, [10.1016/j.lithos.2012.04.004](https://doi.org/10.1016/j.lithos.2012.04.004).
- 537 Waters, D.J., and Martin, H.N. (1993) Geobarometry in phengite-bearing eclogites. *Terra Abstracts*,
538 5:410-411.
- 539 White, E.W. and White, W.B. (1967) Electron microprobe and optical absorption study of colored
540 kyanites. *Science* 158, 915-922.
- 541 Zack, T., Moraes, R. and kronz, A. (2004) Temperature dependence of Zr in rutile: an empirical
542 calibration of a rutile thermometer. *Contributions to Mineralogy and Petrology* 148, 471-488

543

LIST OF FIGURE CAPTIONS

544

545 **Figure 1. (a)** Schematic map of the Saualpe-Koralpe-Pohorje domain (modified from Miller et al.,
546 2007) showing the distribution of regions overprinted by greenschist, amphibolite and eclogite facies
547 metamorphic conditions; major eclogite bodies are displayed by filled ellipses; **(b)** Simplified
548 geological map of the Pohorje Mountains and adjacent areas (modified after Mioč and Žnidarčič, 1977
549 and Janák et al., 2004); the sampling area is indicated by the dashed rectangle in the southeastern part
550 of the Pohorje Massif. Major fault systems are represented by bold lines.

551

552 **Figure 2. (a)-(e)** Correlation plots of selected major and trace elements for Cr-spinel-bearing (PM22:
553 black star; PM26: open star) and Cr-spinel-free (black dots) eclogites from the Slovenska Bistrica area
554 compared to Mg-rich and Mg-poor eclogite bulk compositions from the Koralpe, Saualpe and Pohorje
555 Mountains reported by Miller et al. (2007) (M07) and Sassi et al. (2004) (S04); field boundaries in **(a)**
556 according to Pearce (1983); $Mg\# = [100 * Mg / (Mg + Fe_{tot}^{2+})]$

557

558 **Figure 3.** Optical photomicrographs of Cr-rich assemblages; (a) cluster of turquoise-colored Cr-bearing
559 kyanites enclosing vermicular Cr-spinel grains from sample PM22; note the zonal coloring which is
560 most intense in the immediate vicinity of the Cr-spinel inclusions where Cr contents of kyanite are
561 highest; (b) turquoise-colored Cr-bearing kyanites and pink Cr-bearing corundum forming the inner
562 portion of a reaction corona around a large Cr-spinel grain from sample PM26; the outer portion of the
563 corona consists of pale-green Cr-pargasite which may contain relics of omphacite and garnet indicating
564 a reaction $Cr\text{-spinel} + omphacite + garnet + H_2O = kyanite + corundum + pargasite$.

565

566 **Figure 4.** back-scattered electron (BSE) images showing selected microtextures of eclogite-facies

567 assemblages affected by subsequent retrograde overprint; **(a)** weakly retrogressed domain of Cr-
568 kyanite-bearing sample PM22 with omphacite and garnet mantled by narrow symplectitic rims of
569 Amp+Di+Plag (symp I) and of Amp+Plag (symp II), respectively. Symplectites around kyanite consist
570 of Crn+Spl+Pl (symp III). **(b)** High-Mg coronitic eclogite PM26 containing abundant garnet with
571 kyanite and omphacite inclusions. Incipient retrogressive breakdown of omphacite to form symp I
572 assemblages can be observed in the upper center. **(c)** complex symplectite corona around kyanite: 1)
573 the main part contains Crn+An₉₀, Spr+An₉₀ and Spl+An₉₀ symplectites which are surrounded by a thin
574 An₅₀ rim. **(d)** texturally primary amphibole from sample PM22 with a thin symplectitic reaction rim
575 towards coexisting omphacite (symp V); **(e)** Phengite surrounded by a symplectite Pl+Bt rim (symp
576 IV); **(f)** two textural types of corundum from sample PM26; Crn-I forms lath-shaped poikilitic matrix
577 grains up to 300 µm in size whereas Crn-III is found as part of reaction coronas around Cr-spinel grains
578 associated with Cr-rich kyanite and Cr-rich pargasite; a third textural type of Crn (Crn-II) forms tiny
579 needles which are part of symplectite rims around kyanite (see Fig. 3c).

580

581 **Figure 5.** BSE image and Al, Cr, and Fe X-ray maps of Cr-rich kyanite from samples PM22. Droplets
582 of Cr-spinels are enclosed in kyanite, which is surrounded by a plagioclase–corundum–Mg-Al-spinel
583 symplectite (symp III). The higher Cr content in kyanite is seen as lighter gray areas around the white
584 spinels in the BSE image and as light bluish to greenish colour in the Cr X-ray map. Dark color (black–
585 blue) indicate low concentrations while green–yellow–red colors indicate higher concentrations.

586

587 **Figure 6.** Range of Cr–Al substitution in kyanite from this study compared to data for Cr-rich kyanites
588 from the literature.

589

590 **Figure 7. (a)** Raman spectra for kyanites with 0.6 and 10.7 wt%. With increasing Cr content the bands

591 show both a broadening and a systematic shift towards lower wave numbers; **(b)** band shift and
592 broadening of three Raman bands as a function of Cr content for kyanites with 0.6, 2.1, 8.9, and 10.7
593 wt% Cr₂O₃.

594

595 **Figure 8.** Compositional variation of spinel from samples PM22 and PM26 in terms of molar Al–Mg–
596 Fe³⁺

597

598 **Figure 9.** Compositional variation of texturally primary and secondary calcic amphiboles from samples
599 PM22 and PM26; primary amphiboles contain low and constant Cr₂O₃ contents in the range 0.10–0.15
600 wt% without any significant Al–Cr variation.

601

602 **Figure 10.** Peak metamorphic *PT* conditions of kyanite eclogite sample PM22 using various mineral
603 equilibria or calibrations (Krogh-Ravna and Terry 2004; Holland and Powell 1998; Brandelik and
604 Massonne 2004; Waters and Martin 1993 in combination with Cpx–Grt exchange thermometer after
605 Krogh 2000). The numbers on reaction curves correspond to reaction number in the text.

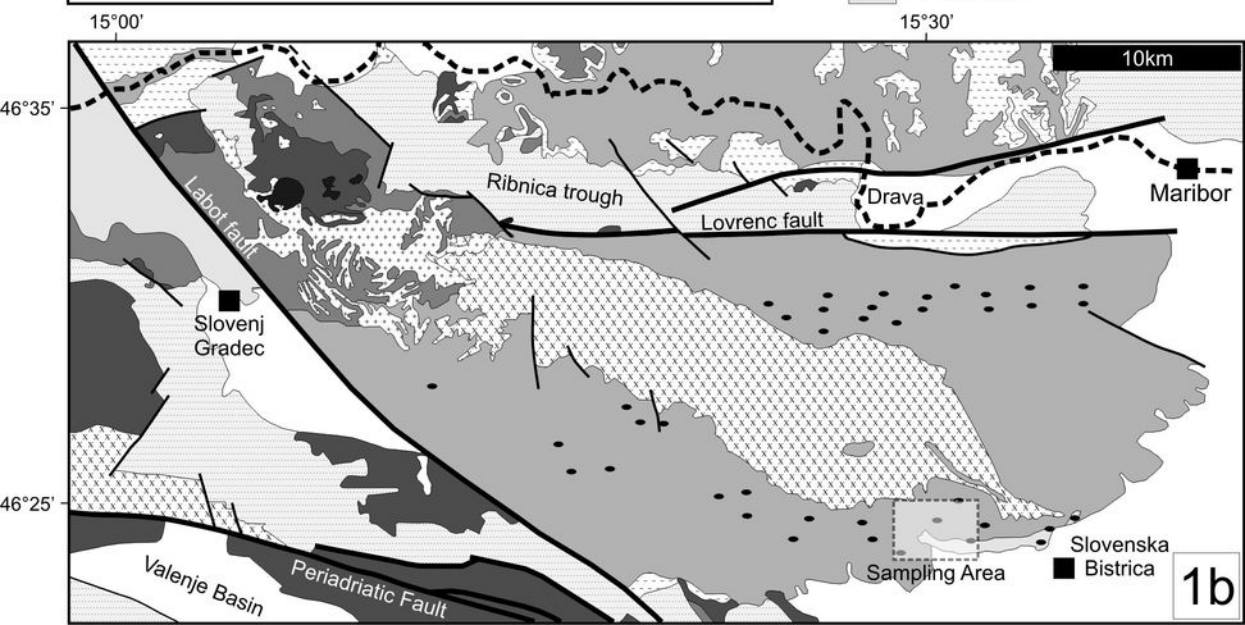
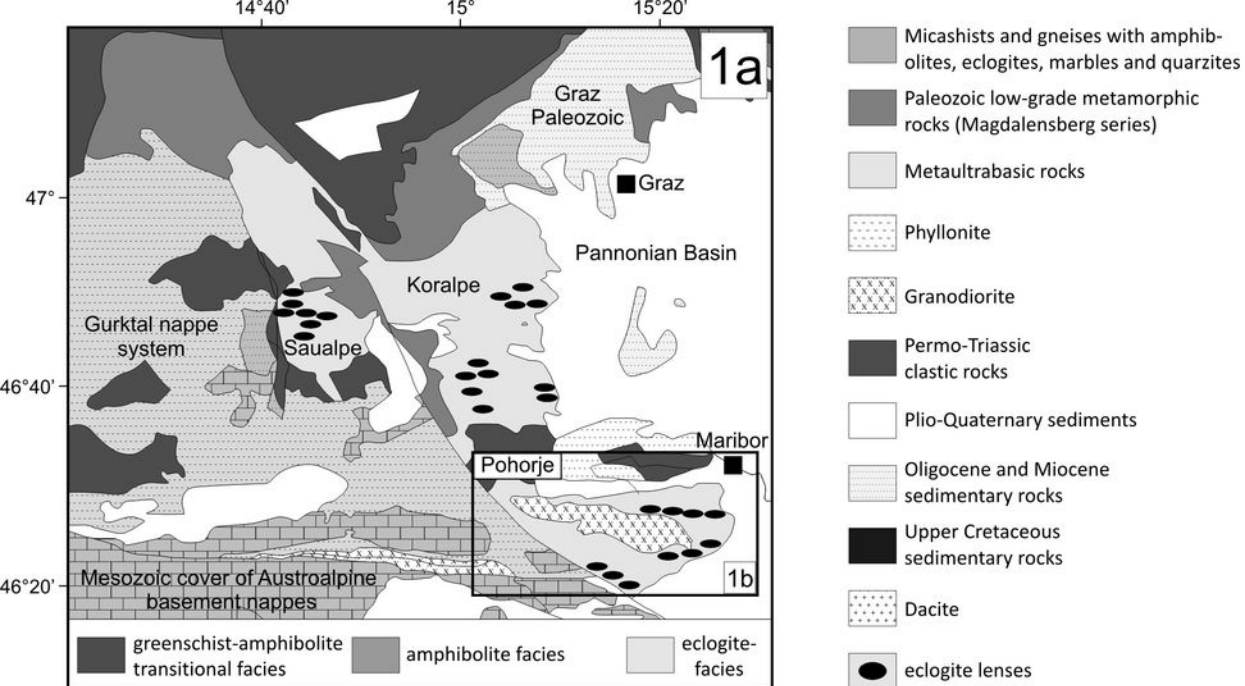
606

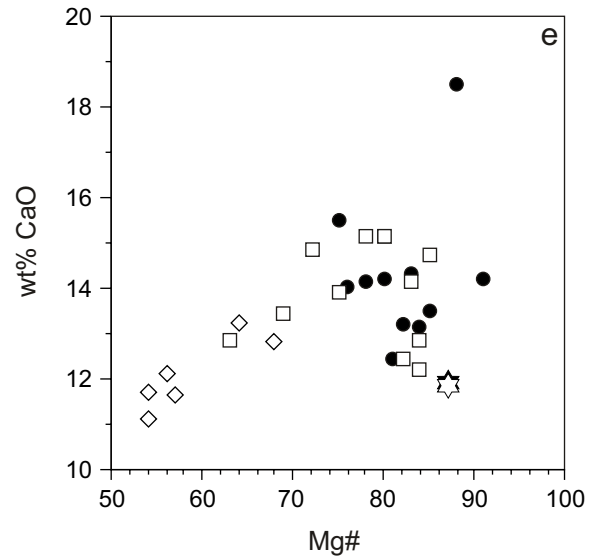
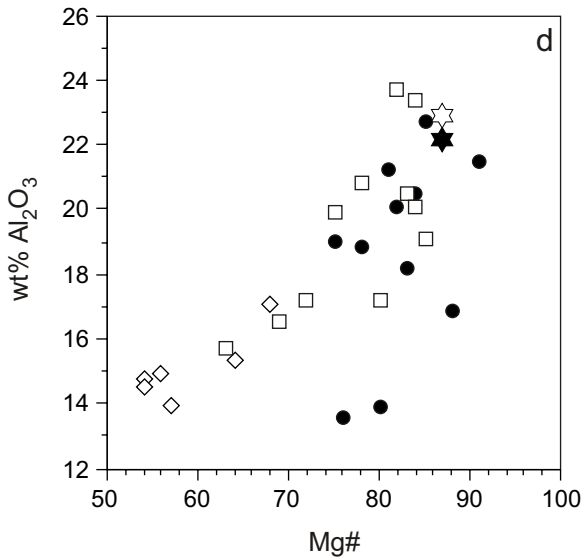
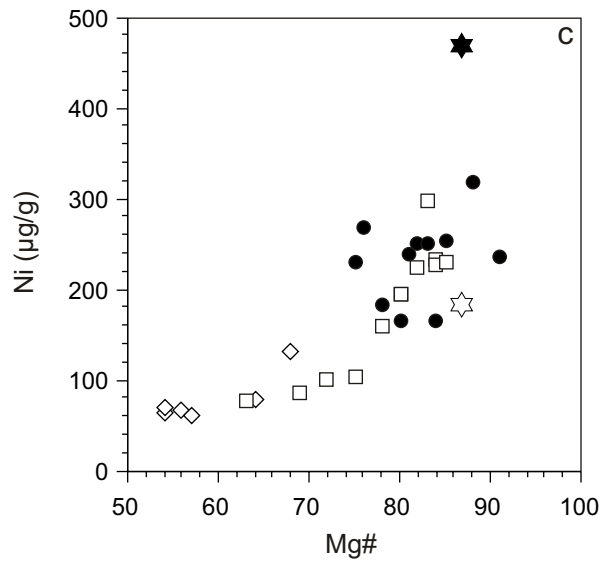
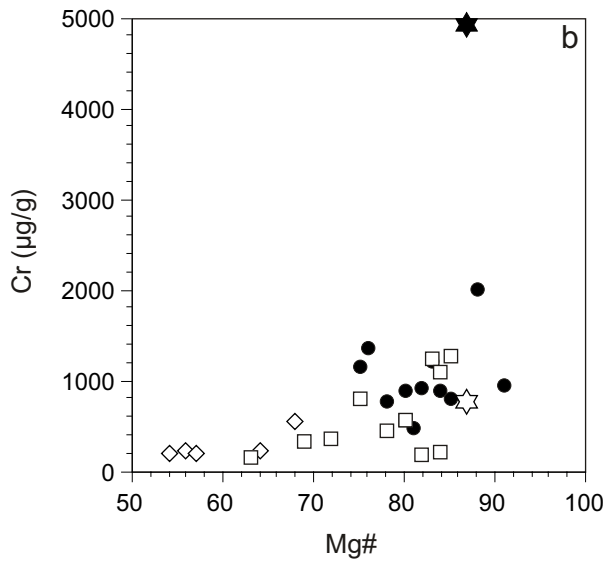
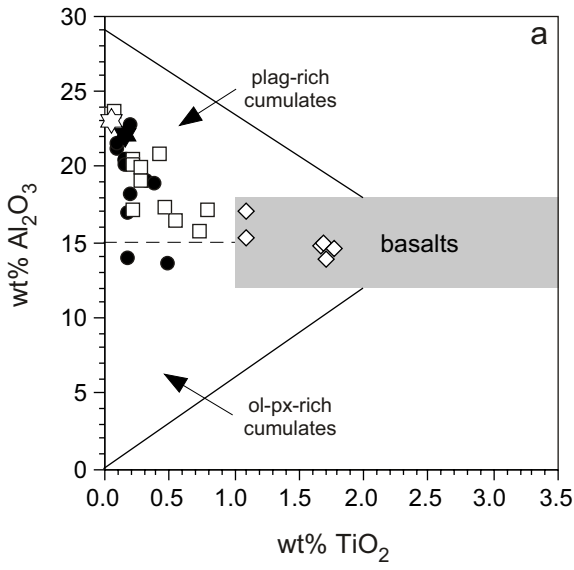
607 **Figure 11.** Calculated Cr-kyanite and Cr-corundum-forming reactions for sample PM26 expressed in
608 terms of endmembers using Perple_X (Connolly, 1990) with the thermodynamic dataset of Holland and
609 Powell (1998 and updates). Endmember activity corrections were performed using the program AX_2
610 provided by Tim Holland ($a_{\text{Sp}}: 0.13$; $a_{\text{Ky}}: 0.83$; $a_{\text{Grs}}: 0.08$; $a_{\text{Prg}}: 0.35$; $a_{\text{Cor}}: 0.9$; $a_{\text{Prg}}: 0.30$; $a_{\text{Jd}}: 0.32$). **(a)**
611 *PT* diagram with Cr-kyanite and Cr-corundum-forming reactions. Reactions 2 and 4 produce kyanite
612 and pargasite at or close to peak *PT* conditions. Along an assumed exhumation path corundum forms at
613 lower *PT* conditions. Stippled lines are calculated with lower $X_{\text{H}_2\text{O}}$. **(b)** Simplified isothermal and
614 isobaric $\mu\text{SiO}_2 - \mu\text{Na}_2\text{O}$ diagram reproducing the observed formation of Ky, Prg, and Cor. Locally

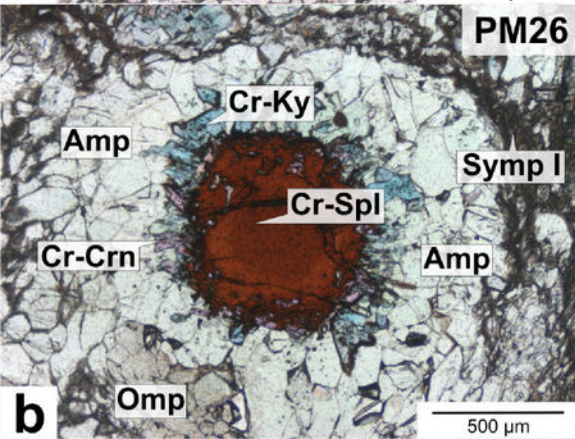
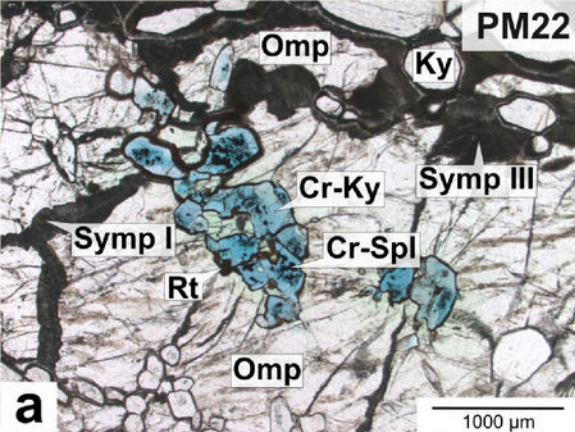
615 reduced SiO_2 activity was responsible for Cor formation ($K_y = \text{Cor}$).

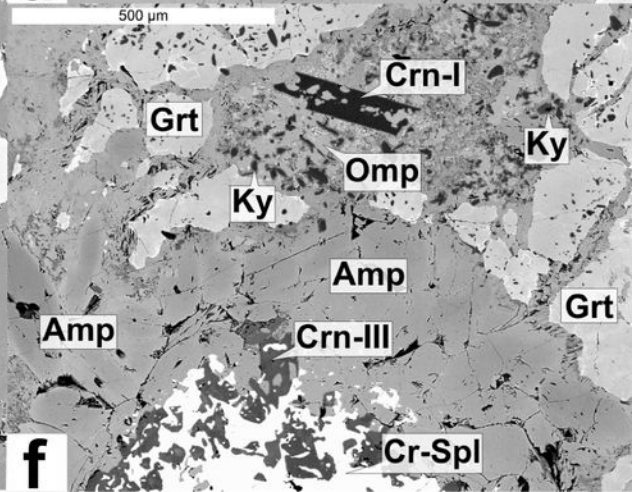
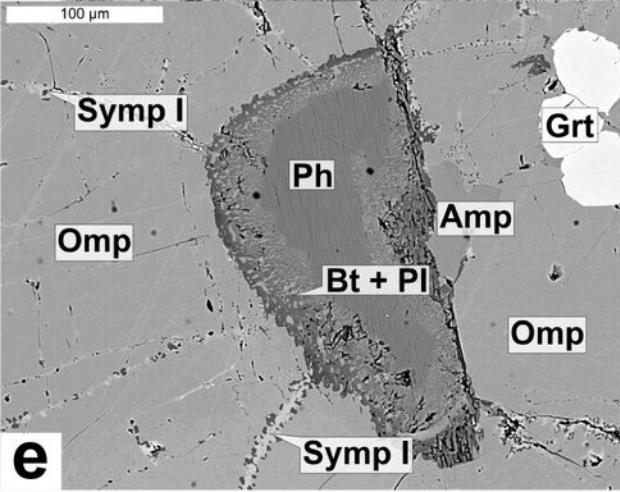
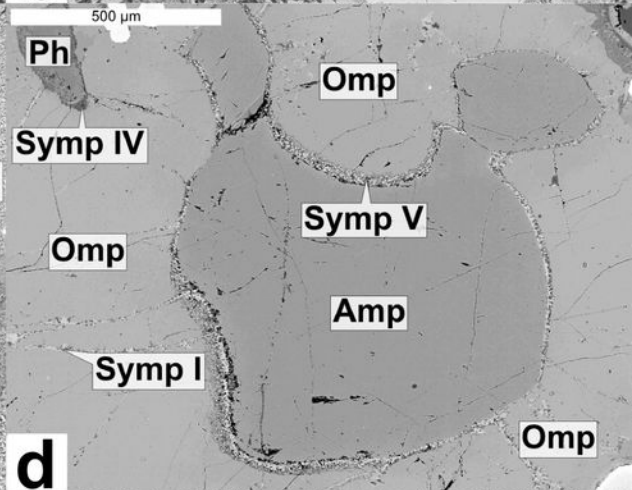
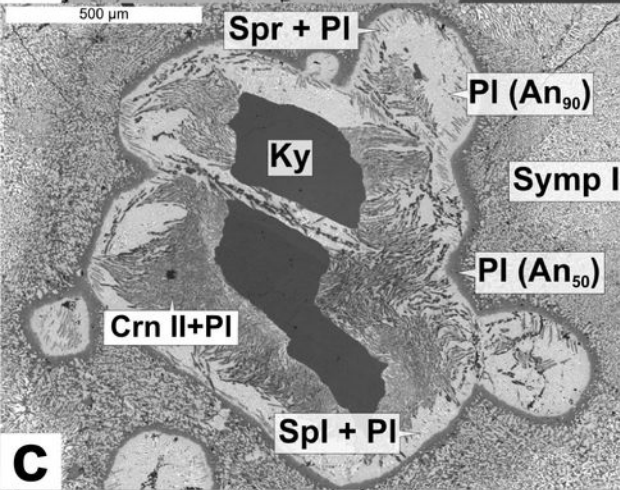
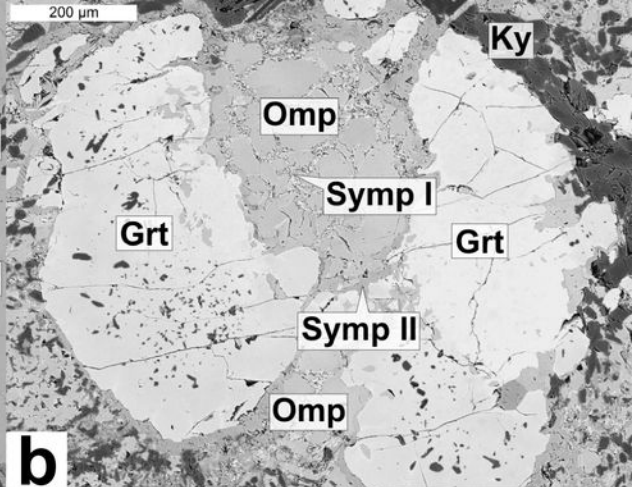
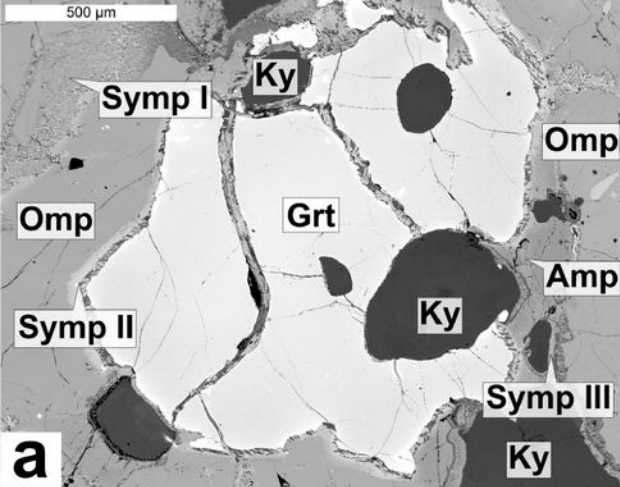
616

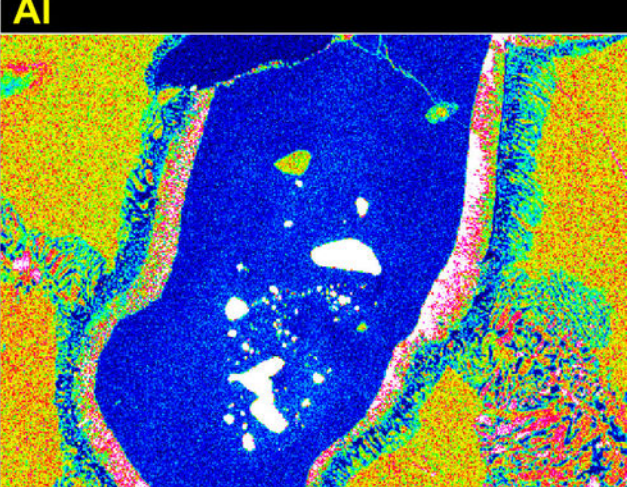
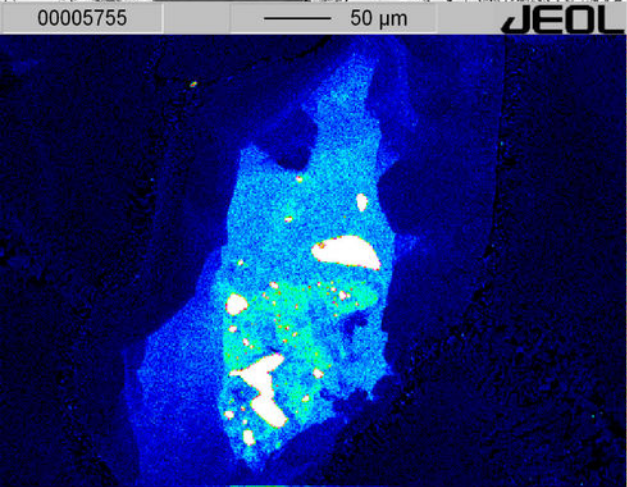
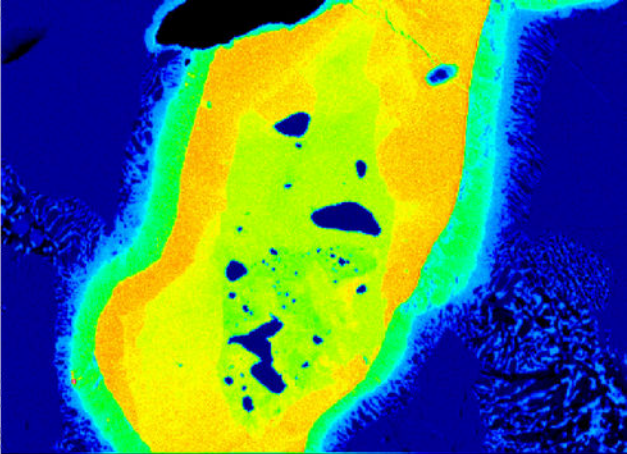
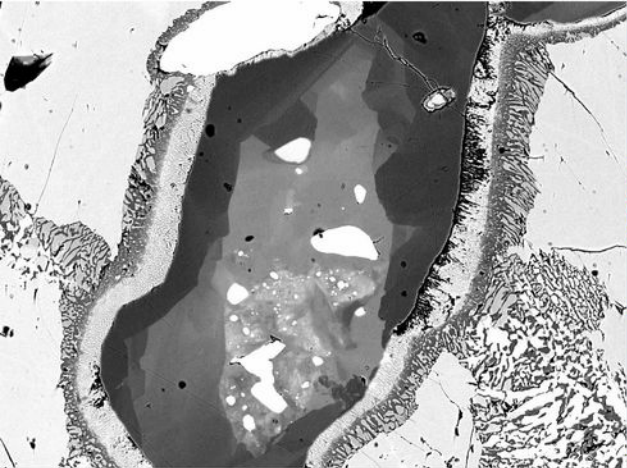
617 **Figure 12.** Sketch explaining the formation of observed spherical coronas around Cr-spinel: (a)
618 Crystallization of eclogite facies assemblage where Cr-spinel remained as magmatic cumulate phase
619 unaffected. (b) Infiltration of H_2O -rich fluids ($+\text{SiO}_{2,\text{aq}}$, $+\text{NaCl}_{\text{aq}}$) during onset of exhumation
620 increasing chemical potential of SiO_2 which facilitates the breakdown of Cr-spinel. (c) Observed
621 corona in sample PM26 ([Fig. 3](#)).

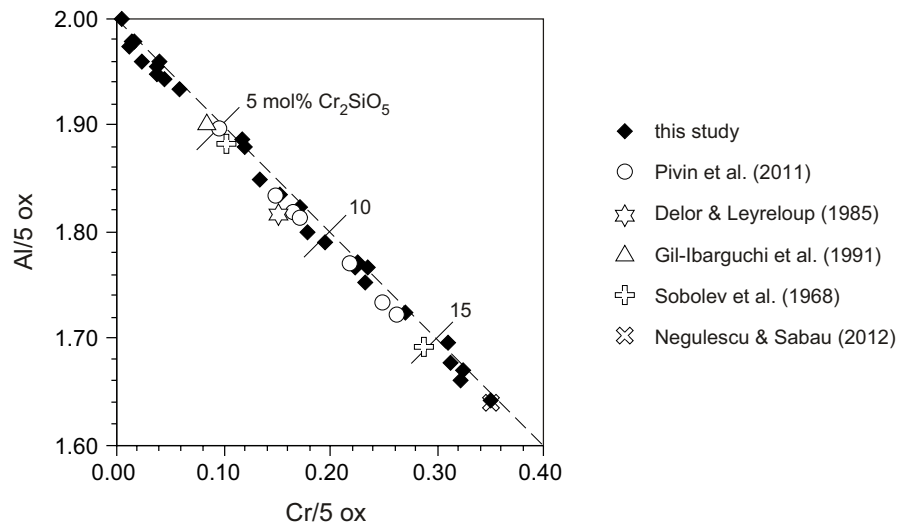


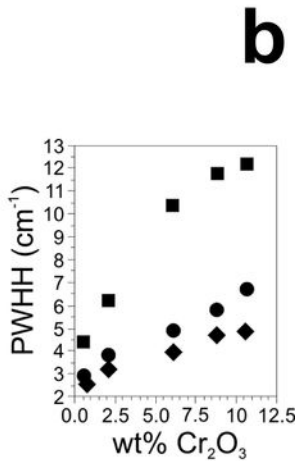
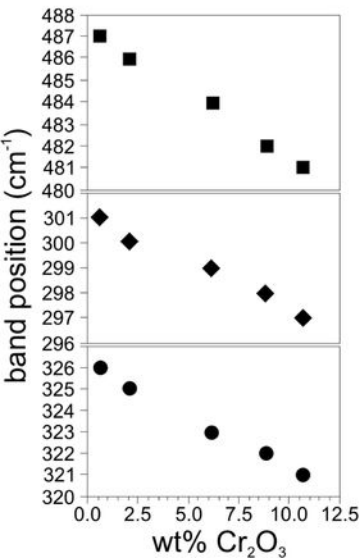
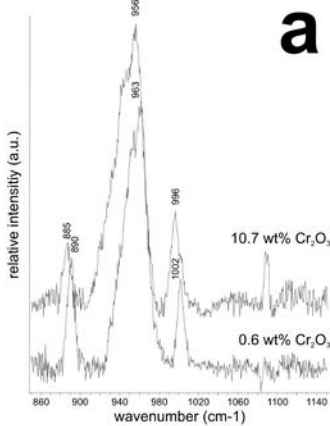
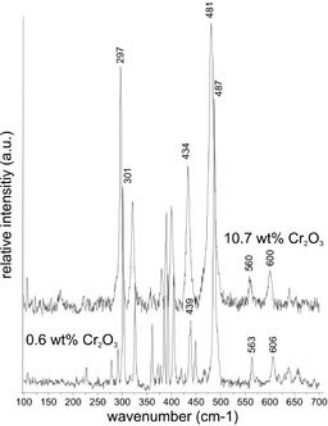


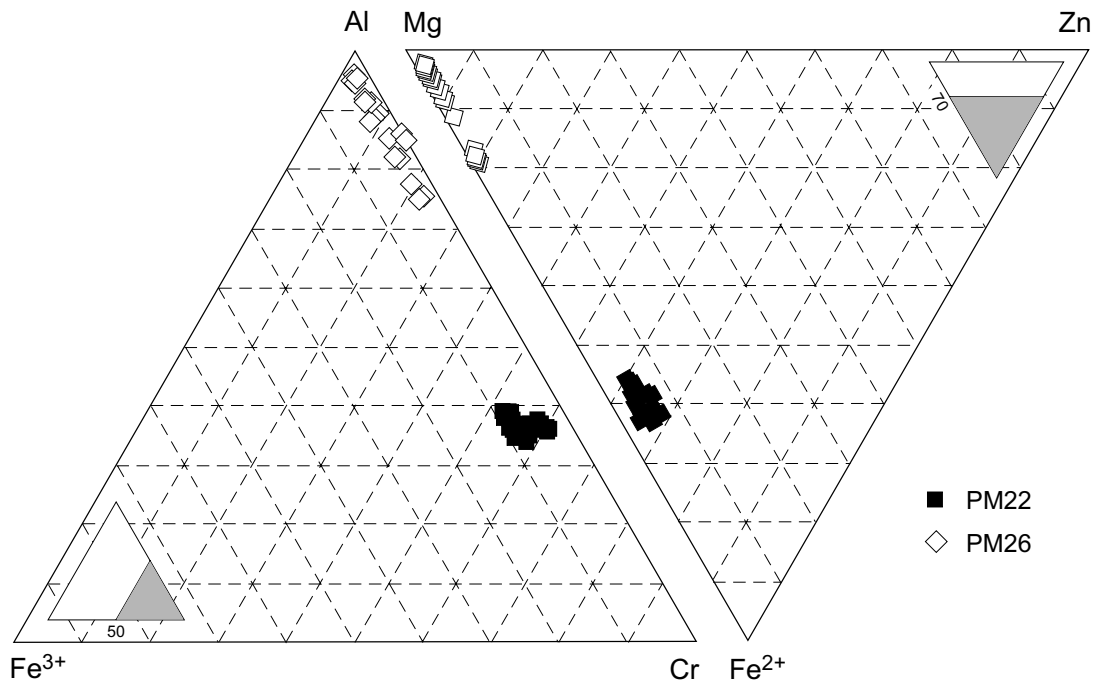


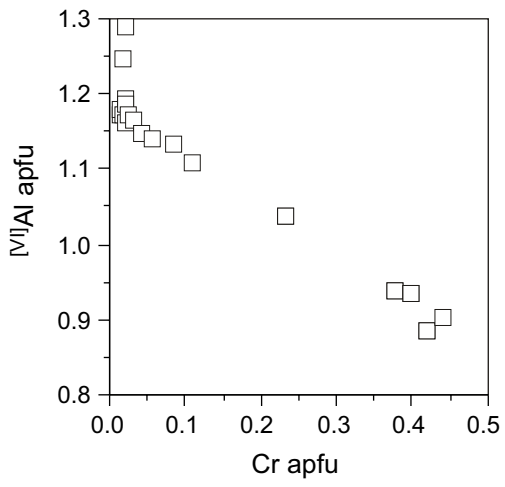
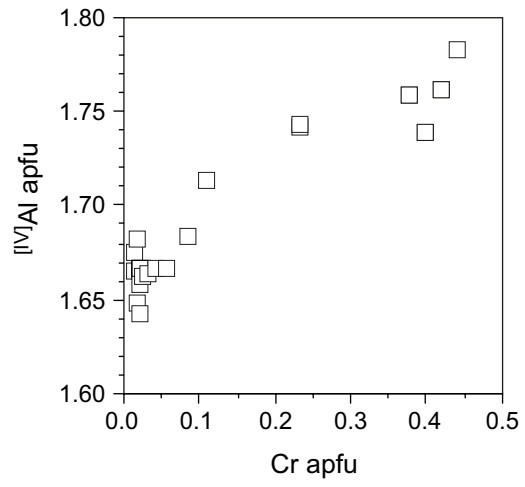
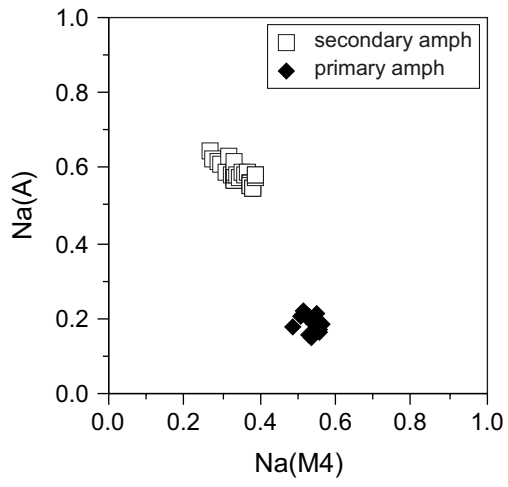


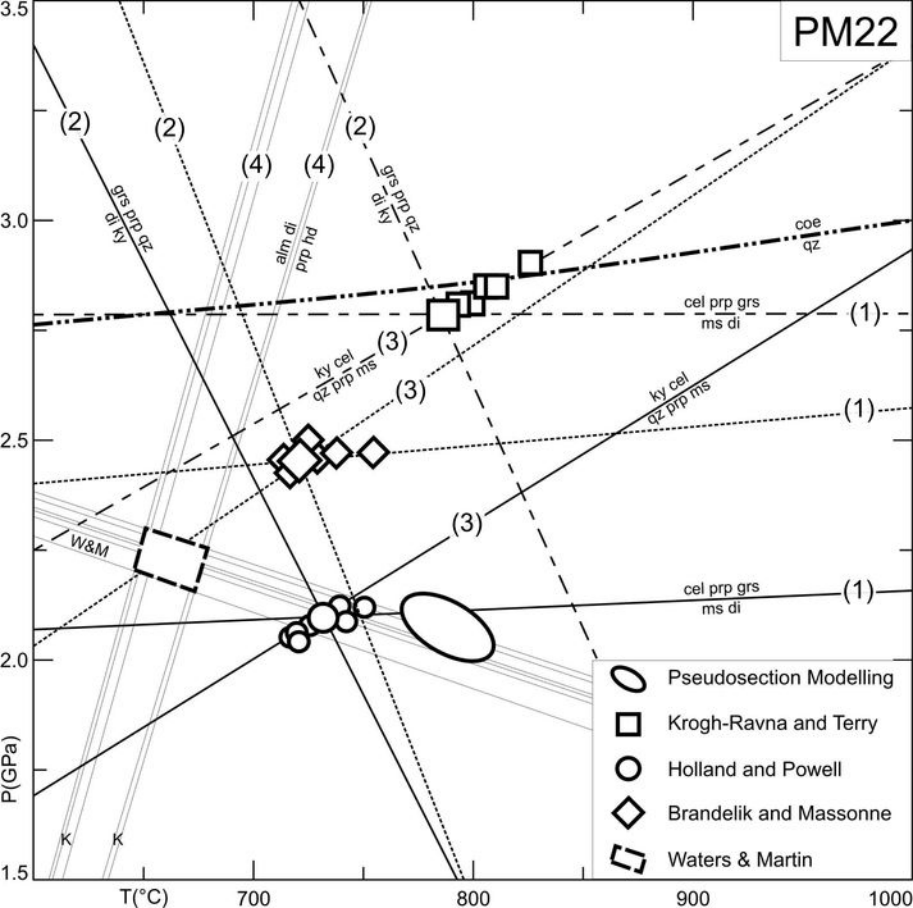


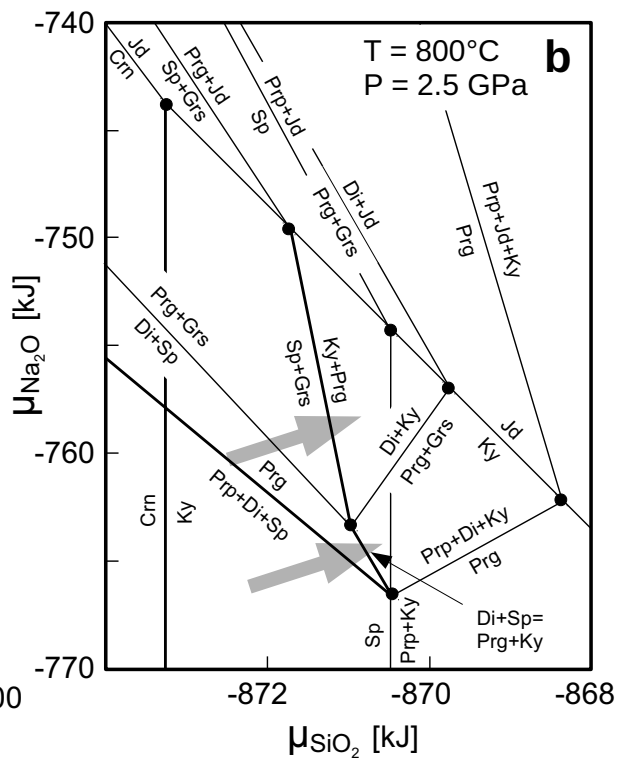
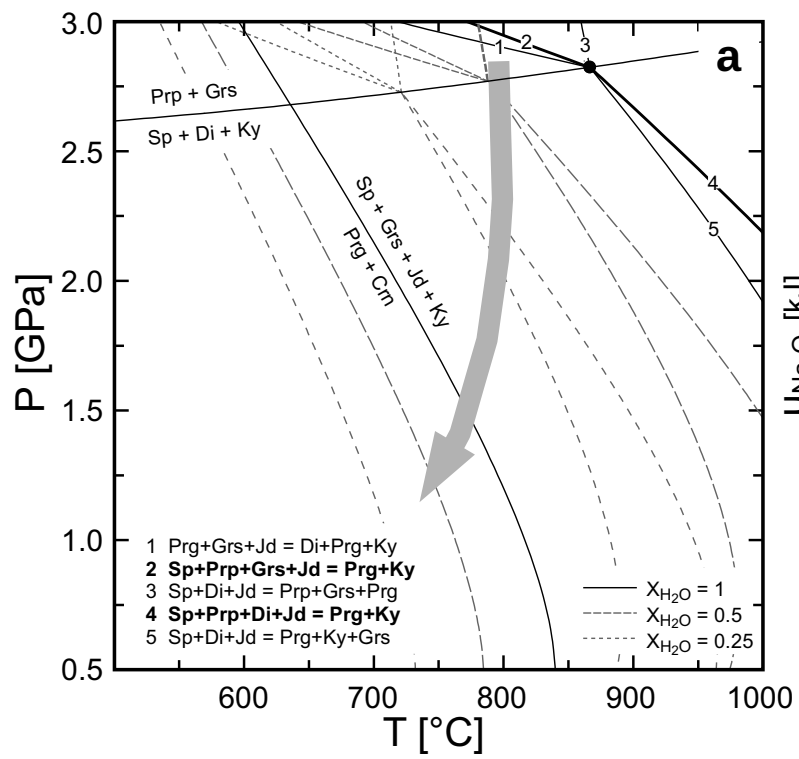












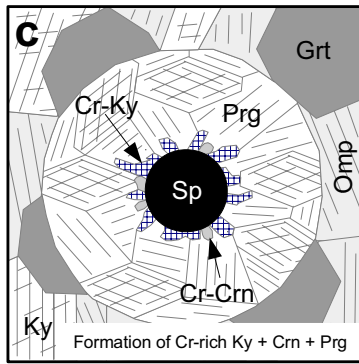
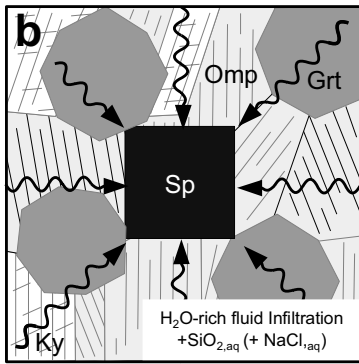
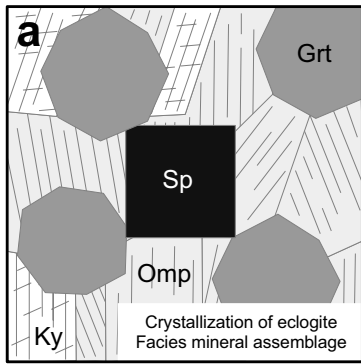


Tabelle1

Table 1. Representative analyses of minerals stable at peak metamorphic conditions from sample PM22

	<i>Omphacite</i>		<i>Garnet</i>				<i>Amphibole</i>		<i>Kyanite</i>	<i>Phengite</i>
	PM22o3	PM22o4	Grt core	Grt rim	Grt core	Grt rim	PM22a7	PM22a10	PM22ky20	PM22ph20
			PM22g94	PM22g180	PM22G109	PM22g14				
SiO ₂	55.00	55.79	39.63	39.90	40.77	39.77	51.40	51.18	38.12	52.04
TiO ₂	0.14	0.14	<0.1	<0.1	<0.1	<0.1	0.37	0.35	<0.02	0.72
Al ₂ O ₃	9.24	9.41	22.76	22.69	23.19	22.94	11.62	11.60	61.19	29.78
Cr ₂ O ₃	<0.1	<0.1	<0.1	<0.1	<0.1	<0.1	0.10	0.11	0.03	0.37
FeO ^{tot}	2.51	2.61	15.66	15.91	14.87	16.07	4.19	4.22	0.37	0.58
MnO	<0.1	<0.1	0.68	0.44	0.53	0.47	<0.01	<0.01	<0.01	<0.1
MgO	11.74	12.25	13.26	13.47	14.06	13.20	16.95	16.94	-	4.04
CaO	16.27	16.11	7.41	7.30	7.31	7.32	9.75	9.76	-	0.11
K ₂ O	<0.1	<0.1	-	-	-	-	0.60	0.61	-	9.21
Na ₂ O	4.74	4.79	-	-	-	-	2.73	2.86	-	0.29
Sum	99.64	101.10	99.40	99.71	100.73	99.77	97.71	97.63	99.71	97.14
Si	1.960	1.958	2.940	2.949	2.971	2.942	7.074	7.060	1.035	3.347
Ti	0.004	0.004	-	-	-	-	0.038	0.036	-	0.035
Al	0.388	0.389	1.990	1.977	1.992	2.000	1.885	1.886	1.957	2.257
Cr	-	-	-	-	-	-	0.011	0.012	0.001	0.019
Fe ³⁺	0.011	0.013	0.130	0.124	0.066	0.117	0.237	0.226	0.008	-
Fe ²⁺	0.064	0.063	0.842	0.859	0.840	0.877	0.245	0.261	-	0.031
Mn	-	-	0.043	0.028	0.033	0.029	-	-	-	-
Mg	0.624	0.641	1.466	1.484	1.527	1.455	3.477	3.483	-	0.387
Ca	0.621	0.606	0.589	0.578	0.571	0.580	1.438	1.442	-	0.008
K	-	-	-	-	-	-	0.105	0.107	-	0.756
Na	0.328	0.326	-	-	-	-	0.728	0.765	-	0.036
Sum	4.000	4.000	8.000	7.999	8.000	8.000	15.238	15.278	3.001	6.876
X _{Jd}	0.346	0.350	X _{Prp}	0.499	0.503	0.514	0.495	X _{Mg}	0.934	0.930
X _{Mg}	0.907	0.911	X _{Grs}	0.200	0.196	0.192	0.197			
			X _{Alm}	0.286	0.291	0.283	0.298			
			X _{Sps}	0.015	0.009	0.011	0.010			
			X _{Mg}	0.635	0.633	0.645	0.624			

Tabelle1

Table 2. Representative analyses of minerals stable at peak metamorphic conditions from sample PM26

	<i>Omphacite</i>		<i>Garnet</i>				<i>Amphibole</i>	<i>Kyanite</i>	<i>Corundum</i>	<i>Zoisite</i>
	PM26o3	PM26o14	Grt rim	Grt rim	Grt core	Grt core	PM26a1	PM26_ky32	PM26k23	PM26zo1
			PM26g7	PM26g142	PM26g7	PM26g14				
SiO ₂	54.59	54.59	42.07	42.14	42.10	41.78	45.73	38.17	-	41.39
TiO ₂	<0.1	<0.1	<0.1	<0.1	<0.1	<0.1	0.13	<0.01	<0.05	<0.1
Al ₂ O ₃	9.46	10.40	23.66	23.92	23.32	23.59	17.33	61.42	99.64	31.82
Cr ₂ O ₃	0.11	0.11	<0.1	<0.1	<0.1	0.16	0.30	0.28	0.34	<0.1
FeO ^{tot}	1.02	1.01	7.10	6.97	7.12	6.72	2.42	0.10	<0.05	0.71
MnO	<0.1	<0.1	0.19	0.07	0.17	0.13	<0.01	<0.05	<0.05	<0.2
MgO	12.28	12.68	17.83	18.04	17.21	18.68	16.99	-	-	0.10
CaO	17.84	17.06	9.04	9.06	9.78	8.45	11.18	-	-	24.70
Na ₂ O	4.13	4.19	-	-	-	-	3.44	-	-	-
K ₂ O	<0.2	<0.2	-	-	-	-	0.06	-	-	-
Sum	99.43	100.03	99.89	100.20	99.70	99.51	97.56	99.87	99.98	98.01
Si	1.946	1.929	2.997	2.988	3.012	2.975	6.342	1.033	-	3.108
Ti	-	-	-	-	-	-	0.014	-	-	-
Al	0.397	0.433	1.986	1.999	1.966	1.980	2.832	1.959	2.993	2.816
Cr	0.003	0.003	-	-	-	0.009	0.033	0.006	0.007	-
Fe ³⁺	-	-	0.021	0.024	0.009	0.060	0.140	0.002	-	0.040
Fe ²⁺	0.030	0.030	0.402	0.389	0.417	0.340	0.141	-	-	-
Mn	-	-	0.011	0.004	0.010	0.008	-	-	-	-
Mg	0.653	0.668	1.893	1.907	1.835	1.983	3.512	-	-	0.011
Ca	0.681	0.646	0.690	0.688	0.750	0.645	1.661	-	-	1.987
Na	0.285	0.287	-	-	-	-	0.925	-	-	-
K	-	-	-	-	-	-	0.011	-	-	-
Sum	3.995	3.996	8.000	7.999	7.999	8.000	15.611	3.000	3.000	7.962
X _{Jd}	0.295	0.308	X _{Prp} 0.632	0.638	0.609	0.666	X _{Mg} 0.962			X _{Fe} 0.014
X _{Mq}	0.956	0.957	X _{Grs} 0.230	0.230	0.249	0.217				
			X _{Alm} 0.134	0.130	0.138	0.114				
			X _{Sps} 0.004	0.001	0.003	0.003				
			X _{Mq} 0.825	0.831	0.815	0.854				

TABLE 3. Chemical composition of Cr-rich omphacite and amphibole from samples PM22 and PM26

	Omphacite		Pargasite	Aluminopargasite
	PM22om1	PM26om1	PM26a1	PM26AM8
SiO ₂	54.04	54.39	44.07	45.82
TiO ₂	0.09	<0.05	0.16	0.09
Al ₂ O ₃	7.75	9.37	16.15	16.83
Cr ₂ O ₃	5.24	3.65	3.94	1.50
FeO ^{tot}	2.21	0.77	2.07	2.48
MnO	<0.05	<0.05	0.02	0.02
MgO	10.42	11.06	16.50	16.80
CaO	15.48	16.03	10.65	10.51
Na ₂ O	5.33	5.43	3.54	3.47
K ₂ O	<0.05	<0.05	0.09	0.08
Sum	100.56	100.70	97.19	97.62
Si	1.936	1.923	6.208	6.382
Ti	0.002	-	0.017	0.010
Al	0.327	0.390	2.681	2.762
Cr	0.148	0.102	0.439	0.166
Fe ³⁺	0.019	-	0.000	0.000
Fe ²⁺	0.047	0.023	0.244	0.289
Mn	-	-	0.002	0.002
Mg	0.557	0.583	3.465	3.488
Ca	0.594	0.607	1.607	1.569
Na	0.370	0.372	0.967	0.938
K	-	-	0.016	0.014
Sum	4.000	4.000	15.646	15.620
X _{Mg}	0.922	0.962	0.934	0.923
X _{Na}	0.384	0.380		
X _{Kos}	0.148	0.102		
X _{Jd}	0.203	0.270		
X _{Acm}	0.019	0.000		
X _{Ca-Ts}	0.062	0.060		
X _{Di}	0.532	0.547		
X _{Hd}	0.047	0.023		

TABLE 4. Chemical composition of Cr-rich kyanite, corundum, and spinel from samples PM22 and PM26

	Cr-kyanite					Corundum		Cr-spinel			
	PM22ck1	PM22ck2	Pm22ky2/1	PM26ky1	PM26ky2	PM26k3	PM26k8	PM22sp11	PM22sp12	PM26sp15	PM26sp22
SiO ₂	35.63	35.41	35.13	36.16	36.52	-	-	-	-	-	-
TiO ₂	0.00	0.10	0.00	0.00	0.00	<0.05	<0.05	<0.05	<0.05	<0.05	<0.05
Al ₂ O ₃	49.90	50.29	49.01	55.33	55.10	90.65	91.06	8.86	9.09	26.89	20.45
Cr ₂ O ₃	14.37	13.99	15.60	7.82	8.18	9.07	9.06	57.14	56.60	43.37	49.46
Fe ₂ O ₃	0.50	0.36	0.43	0.27	0.20	<0.05	<0.05	-	-	-	-
FeO ^{tot}	-	-	-	-	-	-	-	27.67	27.44	14.90	17.19
MnO	<0.05	<0.05	<0.05	<0.05	<0.05	-	-	0.14	0.34	0.03	0.09
MgO	-	-	-	-	-	-	-	5.08	4.90	14.56	12.12
ZnO	-	-	-	-	-	-	-	1.40	1.45	0.43	0.43
Sum	100.40	100.15	100.17	99.58	100.00	99.72	100.12	100.28285	99.8199	100.1781	99.7326
Si	1.006	1.001	0.999	1.006	1.012	-	-	-	-	-	-
Ti	-	-	-	-	-	-	-	-	-	-	-
Al	1.661	1.676	1.642	1.814	1.800	1.874	1.875	0.358	0.369	0.946	0.753
Cr	0.321	0.313	0.351	0.172	0.179	0.126	0.125	1.549	1.542	1.024	1.222
Fe ³⁺	0.011	0.008	0.009	0.006	0.004	-	-	0.093	0.089	0.030	0.025
Fe ²⁺	-	-	-	-	-	-	-	0.701	0.702	0.342	0.424
Mn	-	-	-	-	-	-	-	0.004	0.010	0.001	0.002
Mg	-	-	-	-	-	-	-	0.260	0.251	0.648	0.564
Zn	-	-	-	-	-	-	-	0.035	0.037	0.009	0.010
Sum	2.999	2.998	3.001	2.998	2.995	2.000	2.000	3.000	3.000	3.000	3.000
X _{Cr-Ky}	0.161	0.157	0.175	0.086	0.090	X _{Esk} 0.063		X _{Cr} 0.775	0.771	0.512	0.611
						X _{Cor} 0.937		X _{Mg} 0.271	0.263	0.655	0.571

TABLE 5. Chemical composition of rutile inclusions in kyanite and matrix rutile grains (PM22)

	Inclusion in kyanite				Matrix			
	ru-1	ru-2	ru-9	ru-10	ru-6/1	ru-6/2	ru-7/1	ru-7/2
TiO ₂	97.71	97.06	97.42	97.77	99.54	99.13	98.39	98.16
Cr ₂ O ₃	1.62	1.90	1.51	1.46	0.18	0.17	0.25	0.28
Fe ₂ O ₃	0.08	0.04	0.06	0.05	0.31	0.32	0.37	0.38
Sum	99.41	99.00	98.99	99.28	100.03	99.62	99.01	98.82
Ti	0.986	0.984	0.987	0.988	0.996	0.996	0.995	0.995
Cr	0.017	0.020	0.016	0.016	0.002	0.002	0.003	0.003
Fe ³⁺	0.001	0.000	0.001	0.001	0.003	0.003	0.004	0.004
Sum	1.005	1.005	1.004	1.005	1.001	1.001	1.002	1.002
Zr [ppm]	194±34	275±34	236±35	330±34	347±28	403±28	347±28	302±28
Nb [ppm]	289±96	267±96	249±95	206±95	<65	<65	<55	<65